LETTER

https://doi.org/10.1038/s41586-019-1529-0

Mediterranean winter rainfall in phase with African monsoons during the past 1.36 million years

Bernd Wagner[1,35]*, Hendrik Vogel[2,35], Alexander Francke[1,3], Tobias Friedrich[4], Timme Donders[5], Jack H. Lacey[6], Melanie J. Leng[6,7], Eleonora Regattieri[8,9], Laura Sadori[10], Thomas Wilke[11], Giovanni Zanchetta[8], Christian Albrecht[11], Adele Bertini[12], Nathalie Combourieu-Nebout[13], Aleksandra Cvetkoska[5,11], Biagio Giaccio[14], Andon Grazhdani[15], Torsten Hauffe[11], Jens Holtvoeth[16], Sebastien Joannin[17], Elena Jovanovska[11], Janna Just[1,18], Katerina Kouli[19], Ilias Kousis[20], Andreas Koutsodendris[20], Sebastian Krastel[21], Markus Lagos[22], Niklas Leicher[1], Zlatko Levkov[23], Katja Lindhorst[21], Alessia Masi[10], Martin Melles[1], Anna M. Mercuri[24], Sebastien Nomade[25], Norbert Nowaczyk[26], Konstantinos Panagiotopoulos[1], Odile Peyron[17], Jane M. Reed[27], Leonardo Sagnotti[28], Gaia Sinopoli[10], Björn Stelbrink[11], Roberto Sulpizio[29,30], Axel Timmermann[31,32], Slavica Tofilovska[22], Paola Torri[24], Friederike Wagner-Cremer[5], Thomas Wonik[33] & Xiaosen Zhang[34]

Mediterranean climates are characterized by strong seasonal contrasts between dry summers and wet winters. Changes in winter rainfall are critical for regional socioeconomic development, but are difficult to simulate accurately[1] and reconstruct on Quaternary timescales. This is partly because regional hydroclimate records that cover multiple glacial–interglacial cycles[2,3] with different orbital geometries, global ice volume and atmospheric greenhouse gas concentrations are scarce. Moreover, the underlying mechanisms of change and their persistence remain unexplored. Here we show that, over the past 1.36 million years, wet winters in the northcentral Mediterranean tend to occur with high contrasts in local, seasonal insolation and a vigorous African summer monsoon. Our proxy time series from Lake Ohrid on the Balkan Peninsula, together with a 784,000-year transient climate model hindcast, suggest that increased sea surface temperatures amplify local cyclone development and refuel North Atlantic low-pressure systems that enter the Mediterranean during phases of low continental ice volume and high concentrations of atmospheric greenhouse gases. A comparison with modern reanalysis data shows that current drivers of the amount of rainfall in the Mediterranean share some similarities to those that drive the reconstructed increases in precipitation. Our data cover multiple insolation maxima and are therefore an important benchmark for testing climate model performance.

In the Mediterranean borderlands, the amount and temporal extent of precipitation during the winter half-year (October to March) determines the prevailing type of vegetation and water availability for agrarian land use. In recent decades, the reduction in winter precipitation has become a regular phenomenon in this region, with anthropogenic greenhouse gas and aerosol forcing identified as potential contributors[4]. Current climate model simulations, using the Representative Concentration Pathway (RCP) 4.5 and RCP 8.5 scenarios, predict a progressive summer drying over the next century[1]. Precipitation changes during the winter months in the Northern Hemisphere are less well constrained; different simulation runs show trends towards both wetter and drier conditions. The uncertainty in winter precipitation projections limits the extent to which current modelling approaches are useful for decision-makers[5,6].

Long-term, empirical baseline data from proxy records help to constrain uncertainties in climate modelling. Proxy records and modelling experiments suggest that enhanced precipitation in the Mediterranean region is in phase with the northward shift of the intertropical convergence zone (ITCZ) and increase in African monsoon strength during precession minima that cause Northern Hemisphere summer insolation (NHSI) maxima and winter insolation (NHWI) minima[2,7–9]. However, most continental records that are capable of capturing hydroclimate change do not cover multiple NHSI maxima with different underlying orbital geometries. In fact, the majority of records are limited to the Holocene[10,11], yet the Early Holocene NHSI maximum was relatively weak compared with most other Quaternary interglacial periods, owing to lower eccentricity. Continental proxy time series that cover multiple NHSI maxima from the Mediterranean region are scarce[2,3]. Sediment records from the Mediterranean Sea provide continuity throughout the Plio-Pleistocene and capture cessations of deep-water ventilation associated with the formation of prominent, organic-rich sapropel layers[12,13]. Although multiple factors contribute to sapropel formation, increased freshwater input, particularly from the African continent during the NHSI-forced monsoon maxima, is considered the most important[14,15]. Hence, the Mediterranean sapropel record is thought to be an excellent indicator of the relative timing of the increased strength of African monsoons, rather than a direct indicator of precipitation in, and runoff from, the entirety of the Mediterranean region. Reconstructed precipitation increases in the northern Mediterranean borderlands during sapropel formation have been interpreted to be a product of both intensified summer and winter precipitation[15,16]. Modelling experiments explain increased

[1]Institute of Geology and Mineralogy, University of Cologne, Cologne, Germany. [2]Institute of Geological Sciences & Oeschger Centre for Climate Change Research, University of Bern, Bern, Switzerland. [3]School of Earth, Atmospheric and Life Sciences, University of Wollongong, Wollongong, New South Wales, Australia. [4]International Pacific Research Center, University of Hawai'i at Mānoa, Honolulu, HI, USA. [5]Palaeoecology, Department of Physical Geography, Utrecht University, Utrecht, The Netherlands. [6]National Environmental Isotope Facility, British Geological Survey, Nottingham, UK. [7]Centre for Environmental Geochemistry, School of Biosciences, University of Nottingham, Nottingham, UK. [8]Dipartimento di Scienze della Terra, University of Pisa, Pisa, Italy. [9]Institute of Earth Sciences and Earth Resources-Italian National Research Council (IGG-CNR), Pisa, Italy. [10]Dipartimento di Biologia Ambientale, Università di Roma 'La Sapienza', Rome, Italy. [11]Department of Animal Ecology & Systematics, Justus Liebig University Giessen, Giessen, Germany. [12]Dipartimento di Scienze della Terra, Università di Firenze, Florence, Italy. [13]Institut de Paléontologie Humaine, Muséum National d'Histoire Naturelle, CNRS UMR 7194, Paris, France. [14]Istituto di Geologia Ambientale e Geoingegneria – CNR, Rome, Italy. [15]Faculty of Geology and Mineralogy, University of Tirana, Tirana, Albania. [16]School of Chemistry, University of Bristol, Bristol, UK. [17]Institut des Sciences de l'Evolution de Montpellier, Université de Montpellier, CNRS UMR 5554, Montpellier, France. [18]Fachbereich Geowissenschaften, Universität Bremen, Bremen, Germany. [19]Faculty of Geology and Geoenvironment, National and Kapodistrian University of Athens, Athens, Greece. [20]Paleoenvironmental Dynamics Group, Institute of Earth Sciences, Heidelberg University, Heidelberg, Germany. [21]Institute of Geosciences, Christian-Albrechts-Universität zu Kiel, Kiel, Germany. [22]Institute of Geosciences and Meteorology, University of Bonn, Bonn, Germany. [23]Institute of Biology, University Ss Cyril and Methodius, Skopje, North Macedonia. [24]Laboratorio di Palinologia e Paleobotanica, Dipartimento di Scienze della Vita, Università di Modena e Reggio Emilia, Modena, Italy. [25]Laboratoire des Sciences du Climat et de l'Environnement, Université Paris-Saclay, CEA/CNRS/UVSQ UMR 8212, Gif-Sur-Yvette, France. [26]Helmholtz Centre Potsdam, GFZ German Research Centre for Geosciences, Potsdam, Germany. [27]Department of Geography, Geology and Environment, University of Hull, Hull, UK. [28]Istituto Nazionale di Geofisica e Vulcanologia, Rome, Italy. [29]Dipartimento di Scienze della Terra e Geoambientali, University of Bari, Bari, Italy. [30]IDPA-CNR, Milan, Italy. [31]Center for Climate Physics, Institute for Basic Science, Busan, South Korea. [32]Pusan National University, Busan, South Korea. [33]Leibniz Institute for Applied Geophysics (LIAG), Hannover, Germany. [34]Institute of Loess Plateau, Shanxi University, Taiyuan, China. [35]These authors contributed equally: Bernd Wagner, Hendrik Vogel. *e-mail: wagnerb@uni-koeln.de

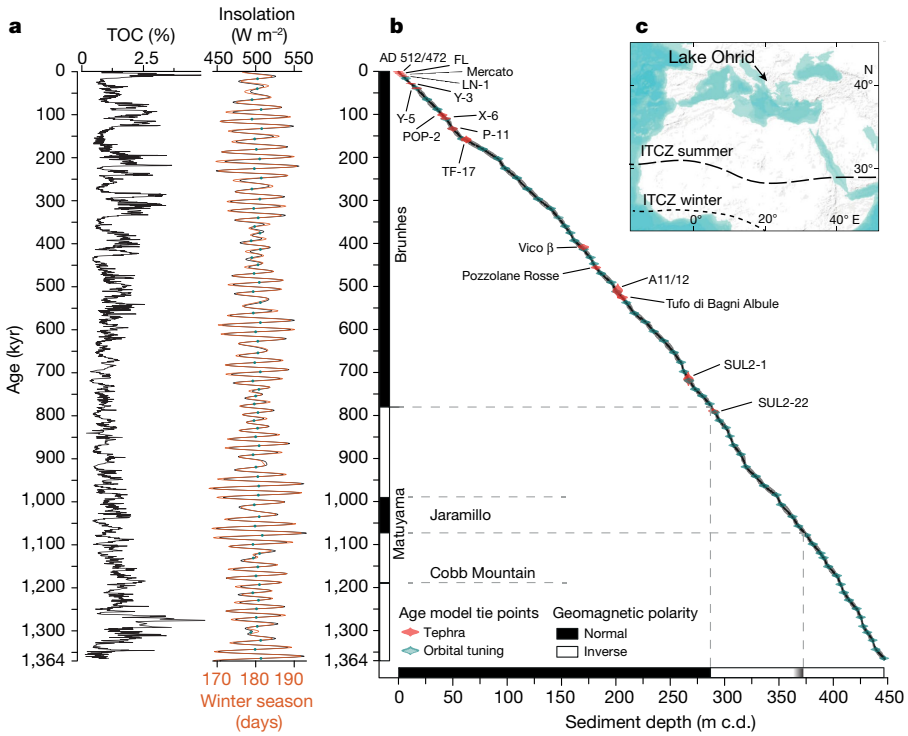

Fig. 1 | Chronology and location of the Lake Ohrid DEEP site record. **a**, Tuning of total organic carbon (TOC) minima in the DEEP site record compared with the inflection points (green dots) in insolation (black line) and winter season length (orange line). **b**, The age model is based on the tephrostratigraphic correlation of the 16 tephra layers to their radiometrically dated proximal deposits (red ellipses, first-order tie points; ages and errors in Extended Data Table 1; see Methods), tuning points (green dots from **a**, second-order tie points; error of ±2,000 years; see Methods) and cross-evaluation of two palaeomagnetic age reversals (dashed lines). Ellipses indicate error ranges. The age modelling followed a previously published methodological approach[20] (see Methods). **c**, Location of Lake Ohrid and the approximate position of the ITCZ in summer and winter. m c.d., m composite depth.

winter precipitation by stronger wintertime storm tracks[2] or a higher air–sea temperature difference, and locally induced convective precipitation that dominate changes in the freshwater budget on obliquity timescales[17]. Alternatively, conceptual models based on proxy time series have suggested that the frequency and intensity of low-pressure systems increase in the Mediterranean region—mostly during fall and early winter[7,8,16]. Thus, a well dated proxy record that covers multiple glacial–interglacial cycles and is sensitive to changes in the Mediterranean hydroclimate is key to addressing long-standing questions regarding the underlying mechanisms, timing and amplitude of precipitation variability under different climate boundary conditions (greenhouse gas concentrations, orbital geometries, and the volume and extent of the continental ice sheets).

Here, we assess precipitation variability in a continuous, independently dated 1.36-million-year (Myr) long sedimentary record from Lake Ohrid (Fig. 1 and Extended Data Fig. 1). Climate variations at this site represent broader climate variability across the northern Mediterranean borderlands[18]. We compare our sedimentary proxy time series with transient climate simulation data and prominent monsoon records, to provide a mechanistic understanding of precipitation variability and seasonality, as well as phase relationships to orbital forcing.

Lake Ohrid is of tectonic origin and 293 m deep. The lake is hydrologically open and primarily fed by an extensive karst aquifer system, which supplies ions (mainly Ca^{2+} and HCO_3^-) to the lake and filters particulate matter[19]. Scientific drilling in 2013 resulted in a 584-m-long composite sediment succession from the lake centre, which consists of fine-grained hemi-pelagic muds[18,20] in the upper 447 m. Sedimentation is thought to have been uninterrupted, with no evidence of unconformities or erosion surfaces. Independent age control derived from 16 interspersed tephra layers in combination with magnetostratigraphy (Fig. 1, Extended Data Figs. 2, 3 and Extended Data Tables 1, 2) provides a robust chronological framework. This framework allows us to match changes in orbital parameters with our proxy data to refine the age–depth relationships. The data demonstrate that the Lake Ohrid record spans the past 1.36 Myr (Fig. 1).

Indicators of detrital input (quartz and potassium), catchment vegetation (arboreal pollen excluding pine and deciduous oaks) and hydrological variability (total inorganic carbon, Ca/K, $\delta^{18}O_{calcite}$ and $\delta^{13}C_{calcite}$) show clear orbital-scale cyclicity, which is also characterized by a precessional (about 21,000-year) component (Fig. 2 and Extended Data Figs. 4–6). The persistence of the orbital cyclicity in our data is widely unaffected by tectonic forcing on basin development and lake ontogeny (Extended Data Fig. 5). During periods of global ice volume minima and NHSI maxima, we observe prominent peaks in the hydrological and vegetation proxy data (Fig. 2). We interpret these peaks in total inorganic carbon (mainly from endogenic calcite) and Ca/K (a proxy for the concentration of calcite) to result from enhanced activity of, and ion supply from, the karst aquifers combined with higher aquatic productivity due to warmer conditions[19]. Pollen analyses show a simultaneous increase in vegetation cover—particularly in deciduous oaks—during early phases of interglacial periods. Deciduous oaks benefit from a limited length of the summer dry season[21]. Lower $\delta^{13}C_{calcite}$ values during these periods suggest greater soil development, whereas lower $\delta^{18}O_{calcite}$ (Extended Data Fig. 4) indicate a more-positive precipitation–evaporation balance[18]. Thus, aquatic and terrestrial datasets suggest that higher temperatures along with maxima in annual precipitation amount and potential shorter summer aridity occurred during interglacial periods (Extended Data Fig. 5).

To provide a better understanding of the observed precipitation variability from the Lake Ohrid record in a regional context, we analysed a climate-data time series derived from a transient 784,000-year simulation using the Earth system model LOVECLIM[22,23] (Extended Data Fig. 7) as well as NOAA (National Oceanic and Atmospheric Administration) reanalysis precipitation data of the Lake Ohrid region for the time period 1979–2017. The temperature time series of the 5° × 5° Lake Ohrid grid cell simulated by the LOVECLIM Earth system

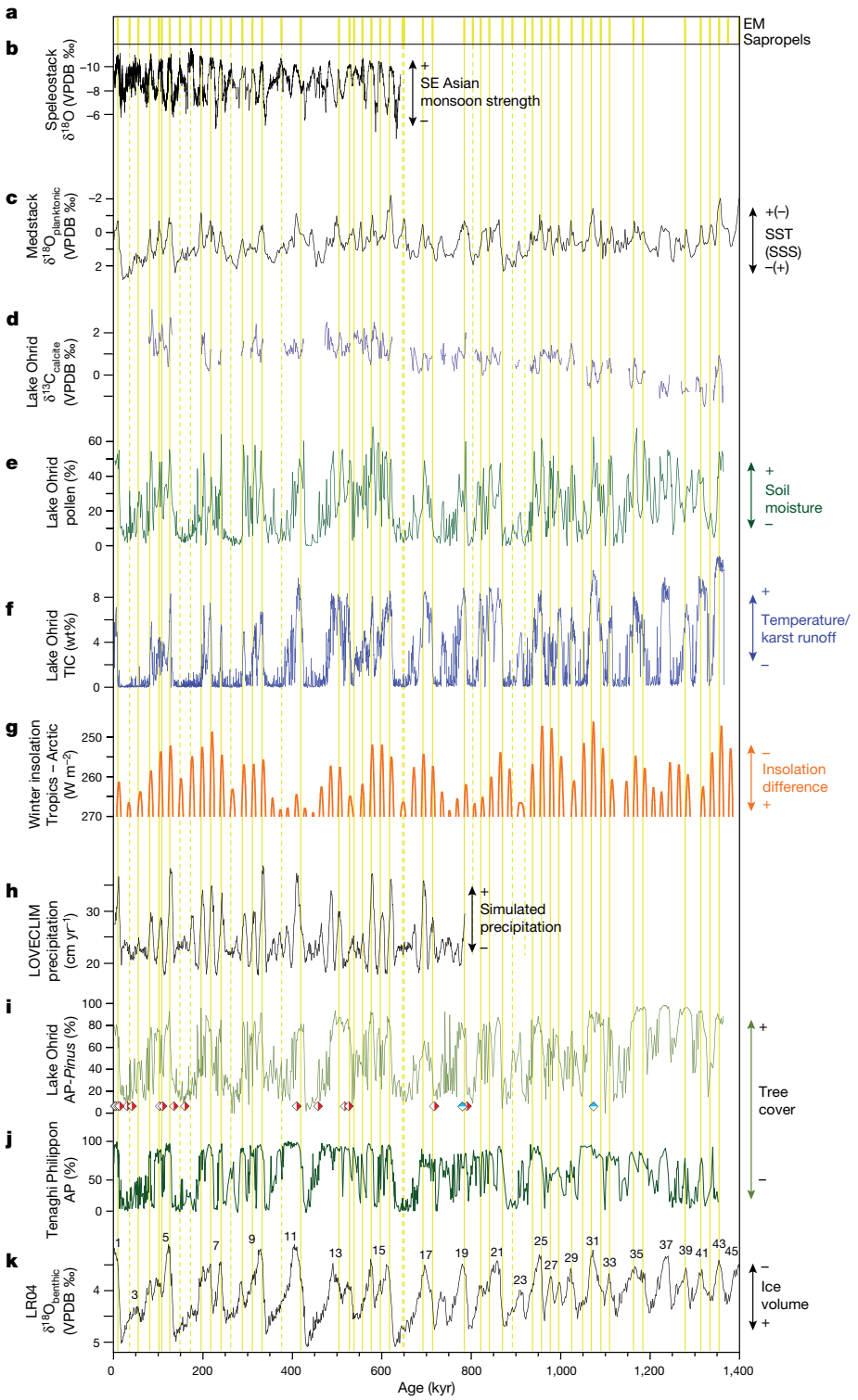

Fig. 2 | Lake Ohrid precipitation indicators and global monsoon records for the past 1.4 Myr. a, Eastern Mediterranean (EM) sapropel ages[12,13,27]. Solid yellow lines indicate good and dashed yellow lines indicate poor/no match with the Ohrid reconstructions. **b**, Chinese speleostack $\delta^{18}O$ isotope ratios[26] in parts per thousand (‰) relative to the Vienna Pee Dee Belemnite (VPDB) scale. **c**, Medstack $\delta^{18}O$ planktonic isotope ratios[28] in parts per thousand relative to VPDB. SSS, sea surface salinity; SST, sea surface temperature. **d**, Lake Ohrid $\delta^{13}C$ endogenic calcite isotope ratios in parts per thousand relative to VPDB. **e**, Percentage of pollen from deciduous oaks at Lake Ohrid. **f**, Lake Ohrid total inorganic carbon (TIC) concentrations. **g**, Difference in Northern Hemisphere winter insolation between the tropic of cancer (23.5°) and the arctic circle[30]. **h**, Annual mean precipitation amount for the Lake Ohrid grid cell from the LOVECLIM simulation. **i**, Percentages of arboreal pollen excluding *Pinus* pollen at Lake Ohrid. **j**, **k**, Percentages of Tenaghi Philippon arboreal pollen (AP)[3] (**j**) and LR04 benthic $\delta^{18}O$ stack isotope ratios[25] in parts per thousand relative to VPDB with odd numbers for interglacial periods (**k**) are shown for comparison. Red and white diamonds indicate the position of radiometrically dated tephra layers, blue and white diamonds the position of reversals of Earth's magnetic field in the Lake Ohrid sediment record. Upward/downward arrows indicate increases (plus) or decreases (minus) in reconstructed climate and environmental variables derived from sedimentary proxies.

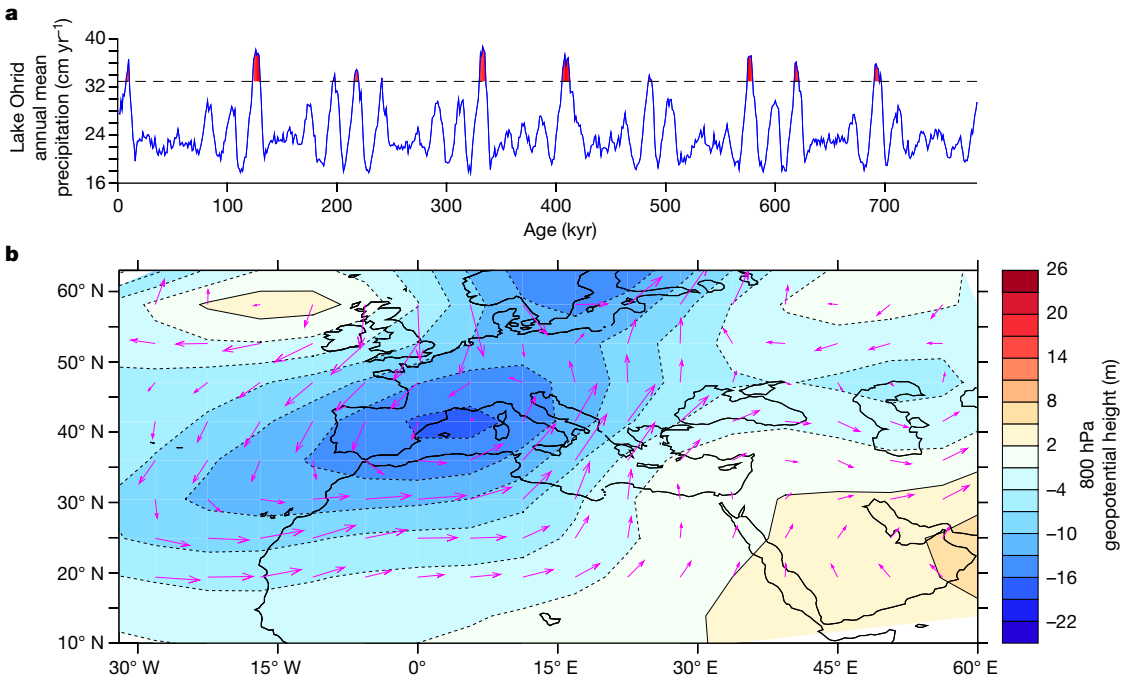

Fig. 3 | Simulated Lake Ohrid precipitation and atmospheric anomaly pattern associated with precipitation maxima. a, Simulated precipitation (cm yr^{-1}) for the Lake Ohrid grid cell. Data based on 1,000-year averages. Dashed line indicates two standard deviations above the mean. Red shading highlights the precipitation values that exceed two standard deviations. See Methods for details on the model simulations. **b**, Composite anomalies of September–November, 800 hPa geopotential height (m, shading) and wind (m s^{-1}, vectors) associated with the precipitation maxima shown in **a**.

model closely resembles the records of the first-order global ice volume (Extended Data Fig. 4), such as the LR04 oxygen isotope stack of marine benthic foraminifera[24] ($r = -0.8737$ or $r^2 = 0.76$ based on 1,000-year averages of both datasets). The fact that it closely matches changes in the amount of detrital siliciclastic sediments and tree pollen (arboreal pollen excluding pine) confirms the sensitivity of the Lake Ohrid record to global-scale climate fluctuations (Fig. 2 and Extended Data Figs. 4, 5). The highest amplitudes in the precipitation time series occur during phases of reduced ice volume, with prominent peaks during NHSI maxima. The significant positive relationship between simulated precipitation and our precipitation proxy time series ($r^2 = 0.38$), and the persistence of the relationship with orbital parameters (Extended Data Fig. 5), indicates that the local response recorded at Lake Ohrid also captures changes in regional hydroclimate back to 1.36 Myr ago (Fig. 2).

The intensification of Northern Hemisphere monsoon systems—which was found both in palaeorecords and in climate model simulations—during precession minima and NHSI maxima is an important example of orbital forcing on changes in precipitation variability[14,15,25]. Iconic records of monsoon strength, such as the Chinese speleothem[26], eastern Mediterranean sapropel[12,13,26] and planktonic foraminifera oxygen isotope records[14,15,27], show a positive phase relationship with the Lake Ohrid hydrological proxy time series (Fig. 2). Strengthening of the monsoons in the Northern Hemisphere results from a northward displacement of atmospheric circulation systems, including the change in position of the Hadley cells and the ITCZ during Northern Hemisphere summer. The shift of the Hadley cells amplifies subsidence over, and persistence of, high-pressure systems in the Mediterranean region, leading to warmer and drier summers[17], and higher sea surface temperatures[16,28]. Reduced NHWI has the highest impact at tropical and subtropical latitudes[2] and leads to low latitude cooling and a southward shift of the ITCZ and the Hadley and Ferrel cells in the Northern Hemisphere. Furthermore, this cooling effect results in a reduced meridional temperature gradient, which leads to a weakening of the westerlies based on the thermal wind relationship. The observed correspondence between the Lake Ohrid precipitation record (Fig. 2 and Extended Data Figs. 4, 5) and the monsoon archives suggests that precipitation increased during the winter half-year of this region when NHWI is low.

The Lake Ohrid record, in combination with the transient simulation time series and the NOAA reanalysis data, may provide fundamental insights into the mechanisms that are invoked by orbital forcing on Mediterranean precipitation. The monthly NOAA reanalysis data of the last 39 years show that high precipitation anomalies (defined as more than two standard deviations above the mean) occur between the months of September and December (Extended Data Fig. 8). The atmospheric pattern associated with these precipitation events exhibits a trough in the Gulf of Genoa region (Extended Data Fig. 8), pointing to either increased cyclogenesis over or advection of North Atlantic low pressure systems into the western Mediterranean region.

The annual cycle of simulated Lake Ohrid precipitation in LOVECLIM is in good agreement with the reanalysis data; however, the model underestimates the annual mean precipitation (Extended Data Fig. 8). Maxima in our simulated precipitation time series (defined as more than two standard deviations above the mean) indicate a positive anomaly from September to November in agreement with the reanalysis data (Fig. 3 and Extended Data Fig. 8). Despite important differences in the geographical expansion of geopotential height anomalies, both the NOAA and LOVECLIM data show pronounced troughs in the central Mediterranean area and an increase in rainfall during the winter half-year in our focus region (Fig. 3). Our observations support previous modelling experiments that suggest that weakened atmospheric stratification and reduced hemispheric temperature contrasts[2], in combination with an increased contrast between warm sea surface temperatures and lower continental air temperatures[17], fuel the increase in precipitation in the Mediterranean. Such a preconditioning is particularly pronounced at the beginning of the fall, when the stronger thermal inertia of the sea relative to the land promotes local cyclogenesis[17,29]. Local cyclogenesis in combination with the southward shift in the atmospheric circulation cells in the Northern Hemisphere during the winter half-year, which also favours a more southerly trajectory for storm tracks across the North Atlantic and into the Mediterranean[2], lead to increased winter rainfall in the Mediterranean mid-latitudes.

Owing to the significant positive correlation between the simulation and our proxy time series (Extended Data Fig. 5) in terms of timing and amplitude, we infer that this mechanism primarily controlled precipitation at Lake Ohrid for the past 1.36 Myr. Indeed, similar to the Northern Hemisphere summer monsoon records, we observe a strong influence of NHSI and a reduced winter temperature contrast in the Northern Hemisphere throughout the entirety of our multiproxy time series, suggesting persistence of the mechanism during different climate boundary conditions. The positive phase relationship between the Lake Ohrid precipitation proxy time series and sapropel records (Fig. 2) indicates a strong coherence of African summer monsoon strength and widespread Mediterranean winter half-year precipitation. Some peaks in our precipitation proxy time series, which are not represented by sapropel layers (Fig. 2), may indicate lower monsoon strength and reduced runoff from the African continent or that the general setting required for sapropel deposition and preservation was not established in the Mediterranean Sea during these periods[15]. During colder and drier glacial periods[3] with increased global ice volume, lower atmospheric CO_2 concentrations and stronger mid-latitude westerlies, insolation forcing on precipitation appears to be suppressed in our record. This is in agreement with the sensitivity simulations conducted to disentangle the individual effects of orbital forcing, Northern Hemisphere ice sheets and CO_2 on Lake Ohrid precipitation (Extended Data Fig. 7).

Precessional forcing on insolation is not only the key driver of the Northern Hemisphere monsoons, but also exerts a strong control on precipitation variability in the Mediterranean mid-latitudes during the Quaternary. Lake Ohrid sediment cores record highly resolved and chronologically well-constrained information on precipitation maxima during phases of lower intrahemispheric temperature contrast and peak sea surface temperatures over the past 1.36 Myr. The apparent equivalence of the past regional key drivers of precipitation extremes to those produced by continued anthropogenic increases in atmospheric greenhouse gas concentrations may help to reduce simulation uncertainties and makes these results also relevant to predictions of the future evolution of the Mediterranean climate.

Online content

Any methods, additional references, Nature Research reporting summaries, source data, extended data, supplementary information, acknowledgements, peer review information; details of author contributions and competing interests; and statements of data and code availability are available at https://doi.org/10.1038/s41586-019-1529-0.

Received: 31 January 2019; Accepted: 28 June 2019;
Published online 2 September 2019.

1. IPCC. *Climate Change 2013: The Physical Science Basis* (eds Stocker, T. F. et al.) (Cambridge Univ. Press, 2013).
2. Kutzbach, J. E., Chen, G., Cheng, H., Edwards, R. & Liu, Z. Potential role of winter rainfall in explaining increased moisture in the Mediterranean and Middle East during periods of maximum orbitally-forced insolation seasonality. *Clim. Dyn.* **42**, 1079–1095 (2014).
3. Tzedakis, P. C., Hooghiemstra, H. & Pälike, H. The last 1.35 million years at Tenaghi Philippon, revised chronostratigraphy and long-term vegetation trends. *Quat. Sci. Rev.* **25**, 3416–3430 (2006).
4. Hoerling, M. et al. On the increased frequency of Mediterranean drought. *J. Clim.* **25**, 2146–2161 (2012).
5. Weisheimer, A. & Palmer, T. N. On the reliability of seasonal climate forecasts. *J. R. Soc. Interface* **11**, 20131162 (2014).
6. Totz, S., Tziperman, E., Coumou, D., Pfeiffer, K. & Cohen, J. Winter precipitation forecast in the European and Mediterranean regions using cluster analysis. *Geophys. Res. Lett.* **44**, 12,418–12,426 (2017).
7. Milner, A. M. et al. Enhanced seasonality of precipitation in the Mediterranean during the early part of the Last Interglacial. *Geology* **40**, 919–922 (2012).
8. Toucanne, S. et al. Tracking rainfall in the northern Mediterranean borderlands during sapropel deposition. *Quat. Sci. Rev.* **129**, 178–195 (2015).
9. Stockhecke, M. et al. Millennial to orbital-scale variations of drought intensity in the eastern Mediterranean. *Quat. Sci. Rev.* **133**, 77–95 (2016).
10. Roberts, N. et al. Stable isotope records of Late Quaternary climate and hydrology from Mediterranean lakes: the ISOMED synthesis. *Quat. Sci. Rev.* **27**, 2426–2441 (2008).
11. Magny, M. et al. North–south palaeohydrological contrasts in the central Mediterranean during the Holocene: tentative synthesis and working hypotheses. *Clim. Past* **9**, 2043–2071 (2013).
12. Emeis, K.-C., Camerlenghi, A., McKenzie, J. A., Rio, D. & Sprovieri, R. The occurrence and significance of Pleistocene and Upper Pliocene sapropels in the Tyrrhenian Sea. *Mar. Geol.* **100**, 155–182 (1991).
13. Kroon, D. et al. Oxygen isotope and sapropel stratigraphy in the Eastern Mediterranean during the last 3.2 million years. In *Proc. Ocean Drilling Program, Scientific Results* Vol. 160 (eds Robertson, A. H. F. et al.) 181–190 (1998).
14. Rossignol-Strick, M. Mediterranean Quaternary sapropels, an immediate response of the African monsoon to variation of insolation. *Palaeogeogr. Palaeoclimatol. Palaeoecol.* **49**, 237–263 (1985).
15. Rohling, E. J., Marino, G. & Grant, K. M. Mediterranean climate and oceanography, and the periodic development of anoxic events (sapropels). *Earth Sci. Rev.* **143**, 62–97 (2015).
16. Tzedakis, P. C. Seven ambiguities in the Mediterranean palaeoenvironmental narrative. *Quat. Sci. Rev.* **26**, 2042–2066 (2007).
17. Bosmans, J. H. C. et al. Precession and obliquity forcing of the freshwater budget over the Mediterranean. *Quat. Sci. Rev.* **123**, 16–30 (2015).
18. Wagner, B. et al. The environmental and evolutionary history of Lake Ohrid (FYROM/Albania): interim results from the SCOPSCO deep drilling project. *Biogeosciences* **14**, 2033–2054 (2017).
19. Vogel, H., Wagner, B., Zanchetta, G., Sulpizio, R. & Rosén, P. A paleoclimate record with tephrochronological age control for the last glacial–interglacial cycle from Lake Ohrid, Albania and Macedonia. *J. Paleolimnol.* **44**, 295–310 (2010).
20. Francke, A. et al. Sedimentological processes and environmental variability at Lake Ohrid (Macedonia, Albania) between 637 ka and the present. *Biogeosciences* **13**, 1179–1196 (2016).
21. Forner, A. et al. Extreme droughts affecting Mediterranean tree species' growth and water-use efficiency: the importance of timing. *Tree Physiol.* **38**, 1127–1137 (2018).
22. Friedrich, T., Timmermann, A., Tigchelaar, M., Elison Timm, O. & Ganopolski, A. Nonlinear climate sensitivity and its implications for future greenhouse warming. *Sci. Adv.* **2**, e1501923 (2016).
23. Timmermann, A. & Friedrich, T. Late Pleistocene climate drivers of early human migration. *Nature* **538**, 92–95 (2016).
24. Lisiecki, L. E. & Raymo, M. E. A Pliocene–Pleistocene stack of 57 globally distributed benthic $\delta^{18}O$ records. *Paleoceanography* **20**, PA1003 (2005).
25. Cheng, H. et al. The Asian monsoon over the past 640,000 years and ice age terminations. *Nature* **534**, 640–646 (2016).
26. Konijnendijk, T. Y. M., Ziegler, M. & Lourens, L. J. Chronological constraints on Pleistocene sapropel depositions from high-resolution geochemical records of ODP sites 967 and 968. *Newsl. Stratigr.* **47**, 263–282 (2014).
27. Colleoni, F., Masina, S., Negri, A. & Marzocchi, A. Plio–Pleistocene high–low latitude climate interplay: a Mediterranean point of view. *Earth Planet. Sci. Lett.* **319–320**, 35–44 (2012).
28. Martrat, B., Jimenez-Amat, P., Zahn, R. & Grimalt, J. O. Similarities and dissimilarities between the last two deglaciations and interglaciations in the North Atlantic region. *Quat. Sci. Rev.* **99**, 122–134 (2014).
29. Trigo, R. M., Osborne, T. J. & Corte-Real, J. M. The North Atlantic Oscillation influence on Europe: climate impacts and associated physical mechanisms. *Clim. Res.* **20**, 9–17 (2002).
30. Laskar, J. et al. A long-term numerical solution for the insolation quantities of the Earth. *Astron. Astrophys.* **428**, 261–285 (2004).

METHODS

Lake and lake hydrology. Lake Ohrid (41° 02′ N, 20° 43′ E, 693 m above sea level (m a.s.l.); Fig. 1c) is located in the sub-Mediterranean climate zone with average monthly air temperatures between 26 °C during summer and −1 °C during winter. Precipitation in the Lake Ohrid watershed increases from 698 to 1,194 mm yr^{-1} with increasing altitude and occurs primarily during winter[31]. The lake is approximately 30 km long, around 15 km wide and has a maximum water depth of 293 m (Extended Data Fig. 1). Sublacustrine karst springs (55%), direct precipitation and river inflow (45%) constitute the water input. Owing to an oligotrophic state, bottom waters remain partly oxygenated for several years, although the lake is oligomictic and a complete overturn occurs only every few years at present[32].

Sediment cores. Sediment cores from the Lake Ohrid DEEP site were recovered in spring 2013, using the Deep Lake Drilling System of Drilling, Observation and Sampling of the Earth's Continental Crust and within the framework of the multinational and interdisciplinary Scientific Collaboration on Past Speciation Conditions in Lake Ohrid (SCOPSCO) project that was co-sponsored by the International Continental Scientific Drilling Program. The composite sediment record[33] is based on six parallel boreholes that reached a terminal depth of 568 m. Sediment recovery from 0 to 456.1 m composite depth (m c.d.) is 99.8%. Small gaps occur between 204.719 and 204.804 m c.d. (8.5 cm) and between 447.89 and 448.19 m c.d. (30 cm)[33]. Mass movement deposits (<3 cm) occur between 117 and 107 m c.d., and between 55 and 50 m c.d. Subsampling in the upper 447.12 m c.d. excluded mass movement and tephra deposits.

Scanning-X-ray fluorescence analysis. Scanning- X-ray fluorescence (XRF) analysis was performed at the University of Cologne on split core surfaces at 2.5-mm increments and 10-s dwell time using an ITRAX XRF core scanner (Cox Analytics) equipped with an energy dispersive silicon drift detector and a Cr tube set to 30 kV and 30 mA. Raw data were processed and element-specific photon energy peaks were integrated in Q-spec (Cox Analytics).

Elemental analysis. Elemental analysis was performed on 16-cm-spaced samples (2,794 samples, around 480 years) following freeze-drying and homogenization at the University of Cologne. For total carbon and TIC measurements, an aliquot of 40 mg of the homogenized sample material was dispersed in 10 ml deionized water. Total carbon was determined at combustion of 900 °C and TIC was measured after treatment with 40% H_3PO_4 at 160 °C using a DIMATOC 100 and a DIMATOC 200 (DIMATEC). TOC content was calculated by subtracting TIC from total carbon.

Fourier transform infrared spectroscopy. Relative concentration changes for quartz were assessed using Fourier transform infrared spectroscopy, on samples spaced at 32 cm (1,462 samples, around 1,000 years). Measurements were performed using a Bruker Vertex 70 equipped with a liquid-N_2-cooled MCT (mercury–cadmium–telluride) detector, a KBr beam splitter and a HTS-XT accessory unit (multisampler) in an air-conditioned laboratory at the University of Bern. In brief, 11 mg of each sample and 500 mg of oven-dried spectroscopic grade KBr (Uvasol, Merck) were homogenized and scanned 64 times at a resolution of 4 cm^{-1} (reciprocal centimetres) for the wavenumber range from 3,750 to 520 cm^{-1} in diffuse reflectance mode. Data processing included a linear baseline correction to remove baseline shifts and tilts by setting two points of the recorded spectrum to zero (3,750 and 2,210–2,200 cm^{-1}). Peak areas diagnostic for symmetric stretching of SiO_4 in quartz (778 and 798 cm^{-1}), and representative for relative abundance[34,35] were integrated using the OPUS (Bruker) software package.

Palynology processing and analysis. Pollen analysis was spaced at 64 cm (697 samples, around 2,000 years) following processing, identification and counting approaches as described previously[36]. Dry sediment (1.0–1.5 g) samples were treated with cold HCl (37 vol%), cold HF (40 vol%) and hot NaOH (10 vol%) to dissolve carbonates, silicates and humic acids, respectively. Glycerin-mounted residues were analysed by transmitted light microscopy to a mean of approximately 533 (including *Pinus*) and around 250 (excluding *Pinus*) grains per sample. Relative abundances are based on the sum of the total terrestrial pollen excluding *Pinus* owing to overrepresentation and potential long-distance transport of this taxon[36]. Deciduous oak abundances represent the combined percentages of *Quercus robur* and *Quercus cerris* types[37], which are commonly used as an indicator for mid-elevation, relatively humid forest across the Mediterranean[38–41].

Isotope analysis. Oxygen and carbon isotopes were analysed on bulk carbonate (calcite)[42] in samples spaced at 16 cm through zones of higher TIC (>0.5%), comprising a total of 1,309 sediment samples. The samples were immersed in 5% NaClO solution for 24 h to gently disaggregate the sediment and oxidize reactive organic material. Potential biogenic carbonate was removed by sieving and the <64-μm fraction was washed with deionized water, dried at 40 °C and then ground to a fine powder in an agate mortar. CO_2 was evolved from 10 mg $CaCO_3$ powders by reaction with anhydrous H_3PO_4 overnight inside a vacuum at a constant temperature of 25 °C. The liberated CO_2 was cryogenically purified under vacuum and collected for analysis on a VG Optima dual inlet mass spectrometer. Oxygen and carbon isotope values are reported in standard delta notation ($\delta^{18}O_{calcite}$ and $\delta^{13}C_{calcite}$, respectively) in parts per thousand calculated to the Vienna Pee Dee Belemnite (VPDB) scale using a within-run laboratory standard (MCS) calibrated against international NBS standards. Analytical reproducibility for the within-run standard was <0.1‰ ($\pm 1\sigma$) for $\delta^{18}O$ and $\delta^{13}C$.

Magnetostratigraphic analyses. Remanent magnetization in its natural state (NRM) and after step-wise alternating field demagnetization (10 steps up to 100 mT) was measured on approximately 900 discrete cube (6.3 cm^3) samples with an average 48-cm spacing at the Paleomagnetic Laboratory at the GeoForschungsZentrum, using a 2G Enterprises cryogenic magnetometer. Palaeomagnetic directions (declination and inclination) were calculated using principle component analysis after removal of low-coercivity magnetic overprints. After identification of geomagnetic polarity transitions, approximately 500 additional samples were taken at 2–3-cm spacing across these transitions for high-resolution analysis at the Istituto Nazionale di Geofisica e Vulcanologia, using the same analytical set-up and routine as at the Paleomagnetic Laboratory. As glacial intervals of the core contain diagenetically formed greigite, which overprints the primary palaeomagnetic signal[43], palaeomagnetic transitions are faithfully preserved only in interglacial intervals, at the base of the Jaramillo sub-Chron (373.8 m c.d.) and at the Matuyama/Brunhes boundary (287.6 m c.d.).

Tephrostratigraphic analysis. Previously, 11 tephra and 3 cryptotephra layers have been identified in the upper 247 m c.d. of the record[44–46]. Furthermore, 2 additional tephra layers from the lower (>247 m c.d.) part of the DEEP site record are introduced here. The tephrostratigraphic correlation of these tephra layers is based on geochemical fingerprinting of single glass shards using wavelength dispersive electron microprobe analysis as described previously[44].

Laser ablation inductively coupled plasma mass spectrometry was used for trace element analyses on single glass shards of OH-DP-2669 and performed at the University of Bonn. The analyses were made with a Resonetics Resolution M50E 193-nm excimer laser ablation system coupled to a Thermo Scientific Element XR, using a spot size of 15–20 μm, a repetition rate of 5 Hz, and a count time of 35 s on the sample after 30 s on the gas blank (background). He (0.75 l min^{-1}) and Ar (around 1.1 l min^{-1}) gas flow transported the ablated material through an in-house signal-smoothing device into the plasma of the inductively coupled plasma mass spectrometer. The signal was tuned to maximum intensity as well as stability at concurrently low oxide ratios (ThO/Th of around 0.0012) to minimize potentially interfering oxide species before analyses in low-resolution mode. Data reduction was performed using an in-house Excel spreadsheet. Trace element concentrations were calculated after calibration against NIST612 using ^{29}Si as the internal standard (Si concentrations were obtained by electron microprobe analysis). Accuracies of the measurements were validated using reference glasses NIST610, T1-G and ATHO-G.

$^{40}Ar/^{39}Ar$ dating was performed at the LSCE facility (CEA, UVSQ and University Paris-Saclay). V5 tephra (that corresponds with OH-DP-2669) was collected at the Montalbano–Jonico section (southern Italy, N40° 17′ 32.8″; E16° 33′ 27.4″). We extracted 20 pristine sanidine crystals of the fraction 0.6–1.0 mm from V5 and irradiated the samples for 2 h in the Cd-lined, in-core CLICIT facility of the Oregon State University TRIGA reactor (Irradiation CO 001). Subsequently, 14 crystals were individually loaded in a copper sample holder and put into a double-vacuum Cleartran window. Each crystal was individually fused using a Synrad CO_2 laser at 10–15% of nominal power (approximately 50 W). The extracted gas was purified for 10 min by two hot GP 110 and two GP 10 getters (ZrAl). Ar isotopes (^{36}Ar, ^{37}Ar, ^{38}Ar, ^{39}Ar and ^{40}Ar) were analysed by mass spectrometry using a VG5400 equipped with an electron multiplier Balzers 217 SEV SEN coupled to an ion counter. Neutron fluence *J* for each sample is calculated using co-irradiated Alder Creek Sanidine (ACs-2) standard with an age[47] of 1.1891 Myr and the total decay constant of a previous publication[48]. *J* values computed from standard grains are 0.00053220 ± 0.00000160 (mean ± s.d.). Mass discrimination was estimated by analysis using an air pipette throughout the analytical period, and was relative to a $^{40}Ar/^{36}Ar$ ratio[49] of 298.56.

Tephra OH-DP-2669 is a 2.5-cm thick, yellowish layer with sharp upper and lower boundaries comprising up to 500-μm large platy glass shards and minor elongated micropumices. Its distinct trachytic composition (Extended Data Fig. 2) and the stratigraphic position between the Matuyama/Brunhes boundary (287.6 m c.d.) and OH-DP-2060 (Tufo di Bagni Albula, 524.84 thousand year (kyr) old[44]; Extended Data Table 1) narrow potential tephrostratigraphic equivalents. Tephra layer SC1-35.30/SUL2-1 from the Sulmona basin in the Italian Apennines is the only tephra with a similar trachytic composition[50,51] for this interval (Extended Data Fig. 2 and Extended Data Table 2). SC1-35.30/SUL2-1 was correlated with tephra V5 from the Montalbano–Jonico section[52,53]. The majority of the SC1-35.30/SUL2-1 and OH-DP-2669 analyses correlate well with the more evolved group of V5 (V5b: SiO_2 > 63 wt%; CaO < 1.5 wt%) and only few analyses plot in the field of the less evolved group V5a (Extended Data Fig. 2 and Extended Data Table 2). Trace-element data of OH-DP-2669 and V5[52] corroborate the correlation (Extended Data Fig. 3). Tephra layers SUL2-1 and V5 were $^{40}Ar/^{39}Ar$ dated to 722.8 ± 2.4 kyr ago[50] and 719.5 ± 12.6 kyr ago[53], respectively. The previous

proposed correlation of SUL2-1/V5 with the Parmenide ash from the Crotone basin[50,52] is not considered here owing to a slightly younger $^{40}Ar/^{39}Ar$ age of the Parmenide ash (710 ± 5 kyr)[54–56] and its geochemical differences to OH-DP-2669 (Extended Data Fig. 2 and Extended Data Table 2).

Tephra OH-DP-2898 is an approximately 0.8-cm thick, whitish-yellowish band of lenses comprising fine-grained glass shards with a high degree of vesicularity and a phonolitic composition (Extended Data Fig. 2). It is located around 2 m below the Matuyama/Brunhes boundary, in calcareous sediments indicative of interglacial conditions[20]. The comparison of the glass composition of OH-DP-2898 with the compositions of Sulmona tephra SUL2-19, SUL2-20, SUL2-25, SUL2-29 and SUL2-31 in a similar magnetostratigraphic position exclude a correlation (Extended Data Fig. 2). Other Sulmona tephra close to the Matuyama/Brunhes transition, SUL2-22, SUL2-23 and SUL2-27, have a composition similar to OH-DP-2898, but SUL2-23 has slightly lower alkali concentration and higher CaO, FeO, TiO_2 concentrations (Extended Data Fig. 2 and Extended Data Table 2). SUL2-27 is geochemically indistinguishable from OH-DP-2898, but deposited in glacial sediments[57] of Marine Isotope Stage (MIS) 20. SUL2-22 is also geochemically indistinguishable from OH-DP-2898 and shares a similar stratigraphic position below the Matuyama/Brunhes boundary[58,59] and at the transition[57] from MIS 20 to MIS 19. A correlation of OH-DP-2898 with tephra V4 from the Montalbano–Jonico section is not possible due to differences in the compositional range (Extended Data Fig. 2 and Extended Data Table 2) and a younger $^{40}Ar/^{39}Ar$ age of 773.9 ± 1.3 kyr of V4[52], quasi-synchronous position during the ^{10}Be peak or Matuyama/Brunhes transition[60]. Furthermore, a correlation of OH-DP-2898/SUL2-22 with tephra V3 of the Montalbano–Jonico section (801.2 ± 19.5 kyr) is excluded due to differences in the geochemical composition (Extended Data Fig. 2 and Extended Data Table 2) and deposition of V3 during glacial conditions[60] of MIS 20. The Pitagora ash from the Crotone basin is in a similar magneto- and climatostratigraphic position[55,61,62], but differs geochemically from OH-DP-2898/SUL2-22. Therefore, we regard the correlation of OH-DP-2898 with SUL2-22 as the most robust and use its $^{40}Ar/^{39}Ar$ age[58] of 791.9 ± 1.9 kyr for our chronology.

In addition to the new tephra correlations, we updated ages for the upper tephra layers (Extended Data Table 1). This includes the Campanian Ignimbrite (Y-5/OH-DP-0169)[63] and tephra layers OH-DP-0404/POP2 and OH-DP-0435/X-6, based on new results from the Sulmona section[64]. The tephrostratigraphy of the Fucino record[65] improved and reassessed the correlations established for OH-DP-0617 and OH-DP-0624[44]. The more precise $^{40}Ar/^{39}Ar$ age (158.8 ± 3.0 kyr) of TF-17, which was correlated to OH-DP-0624, replaced the age of Vico B/OH-DP-0617 (162 ± 6 kyr)[66].

The correlation of cryptotephra OH-DP-1700.6 with the Vico β eruption[45] provided a new chronological tie point at 410 ± 2 kyr ago[67]. The previously established correlation of tephra layer OH-DP-1955 with tephra layer SC-5 from the Mercure basin[44] was rejected in the light of its large uncertainty (±10.9 kyr) and the new tephrostratigraphic data.

Reassessment of the raw Ar-isotope data of SC1-35.30/SUL2-1, the equivalent to OH-DP-2669, by updating the value of the atmospheric Ar-composition ($^{40}Ar/^{36}Ar$: 298.5 instead of 295.5 originally) and removing xenocrysts[58] yielded a new age of 715.02 ± 5.4 kyr (Extended Data Table 1) using the previously published decay constant[48] and an age of 1.1891 Myr for the ACs-2 flux standard[47]. Our new $^{40}Ar/^{39}Ar$ age of V5 (716.2 ± 5.4 kyr; mean square weighted deviation = 0.8, $P = 0.7$) is indistinguishable within uncertainty and thus used for our chronology. All other $^{40}Ar/^{39}Ar$ were recalculated using the software ArAR[68] with a given decay constant and age for ACs-2 (1.1891 Myr)[47] and Fish Canyon sanidines ages[48] of 28.294 Myr.

Chronology. Following the methodological approach for the upper 247 m.c.d. of the record[20], the chronology of the DEEP site sediment succession to 447.12 m.c.d. uses tephrochronological data[44–46] as first-order tie points. Tephrochronological data were used only in cases in which distinctive major element compositions (Extended Data Fig. 2 and Extended Data Table 2) or trace element datasets (Extended Data Fig. 3) allow unambiguous tephrostratigraphic correlations. Trace element datasets of potential tephra equivalents are extremely rare for the period greater than 200 kyr ago, thus limiting the applicability of this valuable tool.

Tuning of climate-sensitive proxy data (TOC; around 480-year resolution) against orbital parameters was used as second-order tie points considering that maxima in TIC represent interglacial periods[19,20]. Some chronologically well-constrained tephra layers deposited at the DEEP site as the penultimate glacial period (Y-5, X-6, P-11 and A11/12) occur at depths at which TOC shows minima at times of the perihelion passage in March[20]. These perihelion passages in March correspond to the inflection points of increasing local summer insolation (21 June) and winter-season length (number of days between the September and March equinoxes) at the latitude of Lake Ohrid (41° N; Fig. 1). Increasing summer insolation promotes high summer temperatures and primary productivity in the water column, and increases organic matter supply to the sediments. An extended winter season improves lake-water mixing that enhances oxidation of organic matter in the water column and the surface sediments[20]. Thus, minima in TOC result from moderate organic matter supply to the sediments and improved oxidation of organic matter at the sediment surface and are used for tuning purposes.

The independent chronological information obtained from the 16 tephra and cryptotephra layers and 66 second-order tie points obtained from orbital tuning were cross-evaluated by the two palaeomagnetic age constraints (base of the Jaramillo sub-Chron and Matuyama/Brunhes boundary; Fig. 1). The age model was calculated using Bacon 2.2[69], considering overall uniform (mem.strength = 60, mem.mean = 0.9, thick = 80 cm) sedimentation rates (acc.shape = 1.5, acc.mean = 20) at the DEEP site[33]. An error of ±2,000 years was applied to the second-order tie points to account for tuning inaccuracy. The 95% confidence intervals of ages for specific depths produced by the Bacon Bayesian age modelling average at ±5,500 years with a maximum of ±10,680 years. The resulting chronology suggests that the upper 447.12 m of the DEEP site record continuously covers the past 1.35 Myr.

We evaluated the chronology of the DEEP site against the U/Th-dated 0–160 kyr-old Soreq Cave[20,70] and 185–250-kyr-old Peqiin Cave speleothem[71] records and found agreement within errors of the chronologies. Arboreal pollen percentages in the DEEP site record are also in agreement with those from the orbitally tuned Tenaghi Philippon record[3] dating to 1.364 Myr ago (Fig. 2).

Model simulations and forcing. Transient simulations with the Earth system model LOVECLIM were conducted to study the effects of orbital forcing, Northern Hemisphere ice sheets and variations in atmospheric greenhouse gases (GHGs) on glacial–interglacial climate change.

LOVECLIM is a coupled ocean–atmosphere–sea-ice–vegetation model[72]. The atmospheric component of LOVECLIM is the spectral T21, three-level model ECBilt[73], which is based on quasi-geostrophic equations that are extended by estimates of ageostrophic terms. The ocean–sea-ice component of LOVECLIM consists of a free-surface Ocean General Circulation Model with a $3° \times 3°$ horizontal resolution coupled to a dynamic–thermodynamic sea-ice model[74]. Atmosphere and ocean components are coupled through the exchange of freshwater and heat fluxes. The vegetation component VECODE[75] of the model computes the evolution of terrestrial vegetation cover based on annual mean surface temperature and precipitation.

The transient simulations of the past 784,000 years were forced by time-dependent boundary conditions for orbital parameters, atmospheric GHG concentrations, Northern Hemisphere ice sheet orography and albedo following the previously published methodology[76]. The orbital forcing was calculated as described previously[77]. Atmospheric GHG concentrations were prescribed according to reconstructions from EPICA Dome C for carbon dioxide[78] as well as methane and nitrous oxide[79]. Orbital forcing and atmospheric GHG concentrations were updated every model year. The effects of Northern Hemisphere ice sheets on albedo and land topography were prescribed according to a previously published study[80]. The forcing was applied with an acceleration factor of 5, which compresses 784,000 forcing years into 156,000 model years. This acceleration factor is appropriate for quickly equilibrating surface variables. The model simulation is an updated version of the one presented in a previous study[76] and uses a higher climate sensitivity, resulting in a better representation of the glacial–interglacial surface temperature amplitude[23].

Four sensitivity simulations were conducted in addition to the full-forcing simulation described above (Extended Data Fig. 7). The sensitivity simulations cover the last four glacial cycles (408,000 years) and aim at exploring the individual effects of atmospheric GHGs, Northern Hemisphere ice sheets and orbital parameters to glacial–interglacial climate change. The first sensitivity simulation uses transient forcing as described above but constant preindustrial atmospheric GHG concentrations. The 'GHG effect' can then be calculated as the difference between the simulation using the full forcing and this simulation. The second sensitivity simulation uses transient forcing as described above but constant preindustrial Northern Hemisphere ice sheets (extent and albedo). The 'Northern Hemisphere ice sheet effect' is calculated as the difference between the full-forcing simulation and this simulation. Two simulations were designed to study the role of orbital forcing under warm and cold climate. For both simulations, transient orbital parameters are used. However, one simulation was run under constant preindustrial atmospheric CO_2 concentration of 280 ppm, whereas the second simulation uses a constant atmospheric CO_2 concentration of 200 ppm, resulting in a colder background climate.

Data analysis. To assess the temporal evolution of dominant periodicities in the DEEP site TIC and deciduous oak pollen percentage data, a wavelet power spectrum was computed for the respective time series. The time series were resampled at regular intervals (linear interpolation) at 0.3 kyr (TIC) and 1.0 kyr (pollen), and subsequently submitted to continuous wavelet transform (Morlet window) using PAST v.3.21 software[81] following the previously published approach[82]. Results of the continuous wavelet transform show clear 100-kyr orbital frequencies over the past 700 kyr, pronounced 41-kyr frequencies before that time and weak approximately

21-kyr orbital frequencies in the pollen record. Relative to the pollen, the continuous wavelet transform results of the TIC show a more-pronounced 100-kyr cyclicity over the entire record, clear presence of 41-kyr periodicity in the early part of the record and very weak 21-kyr signals.

To quantitatively test the observed correlation between deciduous oak and TIC maxima against precession forcing, the bandpass-filtered 18–25-kyr component of the proxy data was regressed against precession based on the La2004 orbital solution[30].

Partial least squares regression (PLSR) was used to test the correlation of TIC and deciduous oaks as predictive variables with LOVECLIM temperature and precipitation output data. PLSR was performed using SIMCA 14 (Sartorius Stedim Biotech). All datasets were filtered using a frequency centred at 0.05 and a bandwidth of 0.02 before multivariate statistical analysis to accommodate for slight age offsets between proxy and simulation data.

We quantitatively assessed the relationships between sapropel occurrence ($n = 53$ for the past 1.4 Myr) and maxima in our Lake Ohrid precipitation proxies. For this analysis, we normalized both TIC and deciduous oak data to 1 and summed the data. Using a peak threshold of 0.5 for this dataset, we defined mid-point ages for precipitation maxima ($n = 93$ for the past 1.36 Myr) and compared their timing to the closest sapropel mid-point ages. Thus, we were able to match 41 precipitation maxima to sapropel mid-point ages (mean age offset of 2.33 kyr (s.d., 1.68); solid yellow lines in Fig. 2). The 10 sapropels for which a match of the Ohrid precipitation signal is absent (dashed yellow lines in Fig. 2) exclusively occur within peak glacial periods.

Data availability

Data are available from the Pangaea database (https://doi.pangaea.de/10.1594/PANGAEA.896848); links to the individual datasets are provided within this dataset. Data used for LOVECLIM are available at https://climatedata.ibs.re.kr/grav/data/loveclim-784k. Additional data are available upon request made to T.F. (tobiasf@hawaii.edu).

Code availability

Model data produced by the LOVECLIM simulations are available through the data centre of the IBS Center for Climate Physics (https://climatedata.ibs.re.kr/grav/data/loveclim-784k).

31. Popovska, C. & Bonacci, O. Basic data on the hydrology of Lakes Ohrid and Prespa. *Hydrol. Processes* **21**, 658–664 (2007).
32. Matzinger, A., Spirkovski, Z., Patceva, S. & Wüest, A. Sensitivity of ancient Lake Ohrid to local anthropogenic impacts and global warming. *J. Great Lakes Res.* **32**, 158–179 (2006).
33. Wagner, B. et al. The SCOPSCO drilling project recovers more than 1.2 million years of history from Lake Ohrid. *Sci. Drill.* **17**, 19–29 (2014).
34. Farmer, V. C. (ed.) *The Infrared Spectra of Minerals* (Adlard & Son, 1974).
35. Chukanov, N. V. *Infrared Spectra of Mineral Species* (Springer, 2014).
36. Sadori, L. et al. Pollen-based paleoenvironmental and paleoclimatic change at Lake Ohrid (south-eastern Europe) during the past 500 ka. *Biogeosciences* **13**, 1423–1437 (2016).
37. Beug, H.-J. *Leitfaden der Pollenbestimmung für Mitteleuropa und angrenzende Gebiete* (Friedrich Pfeil, 2004).
38. Cheddadi, R. et al. Imprints of glacial refugia in the modern genetic diversity of *Pinus sylvestris*. *Glob. Ecol. Biogeogr.* **15**, 271–282 (2006).
39. Rossignol-Strick, M. The Holocene climatic optimum and pollen records of sapropel 1 in the Eastern Mediterranean, 9000–6000 BP. *Quat. Sci. Rev.* **18**, 515–530 (1999).
40. Langgut, D., Almogi-Labin, A., Bar-Matthews, M. & Weinstein-Evron, M. Vegetation and climate changes in the South Eastern Mediterranean during the Last Glacial–Interglacial cycle (86 ka): new marine pollen record. *Quat. Sci. Rev.* **30**, 3960–3972 (2011).
41. Combourieu-Nebout, N. et al. Climate changes in the central Mediterranean and Italian vegetation dynamics since the Pliocene. *Rev. Palaeobot. Palynol.* **218**, 127–147 (2015).
42. Lacey, J. H. et al. Northern Mediterranean climate since the Middle Pleistocene: a 637 ka stable isotope record from Lake Ohrid (Albania/Macedonia). *Biogeosciences* **13**, 1801–1820 (2016).
43. Just, J. et al. Environmental control on the occurrence of high-coercivity magnetic minerals and formation of iron sulfides in a 640 ka sediment sequence from Lake Ohrid (Balkans). *Biogeosciences* **13**, 2093–2109 (2016).
44. Leicher, N. et al. First tephrostratigraphic results of the DEEP site record from Lake Ohrid (Macedonia and Albania). *Biogeosciences* **13**, 2151–2178 (2016).
45. Kousis, I. et al. Centennial-scale vegetation dynamics and climate variability in SE Europe during Marine Isotope Stage 11 based on a pollen record from Lake Ohrid. *Quat. Sci. Rev.* **190**, 20–38 (2018).
46. Francke, A. et al. Sediment residence time reveals Holocene shift from climatic to vegetation control on catchment erosion in the Balkans. *Global Planet. Change* **177**, 186–200 (2019).
47. Niespolo, E. M., Rutte, D., Deino, A. L. & Renne, P. R. Intercalibration and age of the Alder Creek sanidine $^{40}Ar/^{39}Ar$ standard. *Quat. Geochronol.* **39**, 205–213 (2017).
48. Renne, P. R., Balco, G., Ludwig, K. R., Mundil, R. & Min, K. Response to the comment by W. H. Schwarz et al. on "Joint determination of ^{40}K decay constants and $^{40}Ar^*/^{40}K$ for the Fish Canyon sanidine standard, and improved accuracy for $^{40}Ar/^{39}Ar$ geochronology" by P. R. Renne et al. (2010). *Geochim. Cosmochim. Acta* **75**, 5097–5100 (2011).
49. Lee, J. Y. et al. A redetermination of the isotopic abundances of atmospheric Ar. *Geochim. Cosmochim. Acta* **70**, 4507–4512 (2006).
50. Giaccio, B. et al. Revised chronology of the Sulmona lacustrine succession, central Italy. *J. Quat. Sci.* **28**, 545–551 (2013).
51. Giaccio, B. et al. Tephra layers from Holocene lake sediments of the Sulmona Basin, central Italy: implications for volcanic activity in peninsular Italy and tephrostratigraphy in the central Mediterranean area. *Quat. Sci. Rev.* **28**, 2710–2733 (2009).
52. Petrosino, P. et al. The Montalbano Jonico marine succession: an archive for distal tephra layers at the early–middle Pleistocene boundary in southern Italy. *Quat. Int.* **383**, 89–103 (2015).
53. Ciaranfi, N. et al. Integrated stratigraphy and astronomical tuning of lower–middle Pleistocene Montalbano Jonico section (Southern Italy). *Quat. Int.* **219**, 109–120 (2010).
54. Massari, F. et al. Interplay between tectonics and glacio-eustasy: Pleistocene succession of the Crotone basin, Calabria (southern Italy). *Geol. Soc. Am. Bull.* **114**, 1183–1209 (2002).
55. Capraro, L. et al. Climatic patterns revealed by pollen and oxygen isotope records across the Matuyama–Brunhes boundary in the central Mediterranean (southern Italy). *Geol. Soc. Lond. Spec. Publ.* **247**, 159–182 (2005).
56. Capraro, L. et al. Chronology of the lower–middle Pleistocene succession of the south-western part of the Crotone basin (Calabria, southern Italy). *Quat. Sci. Rev.* **30**, 1185–1200 (2011).
57. Giaccio, B. et al. Duration and dynamics of the best orbital analogue to the present interglacial. *Geology* **43**, 603–606 (2015).
58. Sagnotti, L. et al. Extremely rapid directional change during Matuyama–Brunhes geomagnetic polarity reversal. *Geophys. J. Int.* **199**, 1110–1124 (2014).
59. Sagnotti, L. et al. How fast was the Matuyama–Brunhes geomagnetic reversal? A new subcentennial record from the Sulmona basin, central Italy. *Geophys. J. Int.* **204**, 798–812 (2016).
60. Simon, Q. et al. Authigenic $^{10}Be/^{9}Be$ ratio signature of the Matuyama–Brunhes boundary in the Montalbano Jonico marine succession. *Earth Planet. Sci. Lett.* **460**, 255–267 (2017).
61. Rio, D. et al. Reading Pleistocene eustasy in a tectonically active siliciclastic shelf setting (Crotone peninsula, southern Italy). *Geology* **24**, 743–746 (1996).
62. Macrì, P., Capraro, L., Ferretti, P. & Scarponi, D. A high-resolution record of the Matuyama–Brunhes transition from the Mediterranean region: the Valle di Manche section (Calabria, Southern Italy). *Phys. Earth Planet. Inter.* **278**, 1–15 (2018).
63. Giaccio, B., Hajdas, I., Isaia, R., Deino, A. & Nomade, S. High-precision ^{14}C and $^{40}Ar/^{39}Ar$ dating of the Campanian Ignimbrite (Y-5) reconciles the time-scales of climatic–cultural processes at 40 ka. *Sci. Rep.* **7**, 45940 (2017).
64. Regattieri, E. et al. A Last Interglacial record of environmental changes from the Sulmona basin (central Italy). *Palaeogeogr. Palaeoclimatol. Palaeoecol.* **472**, 51–66 (2017).
65. Giaccio, B. et al. First integrated tephrochronological record for the last ~190 kyr from the Fucino Quaternary lacustrine succession, central Italy. *Quat. Sci. Rev.* **158**, 211–234 (2017).
66. Laurenzi, M. A. & Villa, I. $^{40}Ar/^{39}Ar$ chronostratigraphy of Vico ignimbrites. *Period. Mineral.* **56**, 285–293 (1987).
67. Karner, D. B., Marra, F. & Renne, P. R. The history of the Monti Sabatini and Alban Hills volcanoes: groundwork for assessing volcanic–tectonic hazards for Rome. *J. Volcanol. Geotherm. Res.* **107**, 185–219 (2001).
68. Mercer, C. M. & Hodges, K. V. ArAR — a software tool to promote the robust comparison of K–Ar and $^{40}Ar/^{39}Ar$ dates published using different decay, isotopic, and monitor-age parameters. *Chem. Geol.* **440**, 148–163 (2016).
69. Blaauw, M. & Christen, J. A. Flexible paleoclimate age–depth models using an autoregressive gamma process. *Bayesian Anal.* **6**, 457–474 (2011).
70. Grant, K. M. et al. Rapid coupling between ice volume and polar temperature over the past 150,000 years. *Nature* **491**, 744–747 (2012).
71. Bar-Matthews, M., Ayalon, A., Gilmour, M., Matthews, A. & Hawkesworth, C. J. Sea-land oxygen isotopic relationships from planktonic foraminifera and speleothems in the eastern Mediterranean region and their implication for paleorainfall during interglacial intervals. *Geochim. Cosmochim. Acta* **67**, 3181–3199 (2003).
72. Goosse, H. et al. Description of the Earth system model of intermediate complexity LOVECLIM version 1.2. *Geosci. Model Dev.* **3**, 603–633 (2010).
73. Opsteegh, J. D., Haarsma, R. J., Selten, F. M. & Kattenberg, A. ECBILT: a dynamic alternative to mixed boundary conditions in ocean models. *Tellus A Dyn. Meterol. Oceanogr.* **50**, 348–367 (1998).
74. Goosse, H. & Fichefet, T. Importance of ice–ocean interactions for the global ocean circulation: a model study. *J. Geophys. Res.* **104**, 23337–23355 (1999).
75. Brovkin, V., Ganopolski, A. & Svirezhev, Y. A continuous climate–vegetation classification for use in climate–biosphere studies. *Ecol. Modell.* **101**, 251–261 (1997).
76. Timmermann, A. et al. Modeling obliquity and CO_2 effects on Southern Hemisphere climate during the past 408 ka. *J. Clim.* **27**, 1863–1875 (2014).
77. Berger, A. Long-term variations of daily insolation and Quaternary climate change. *J. Atmos. Sci.* **35**, 2362–2367 (1978).
78. Lüthi, D. et al. High-resolution carbon dioxide concentration record 650,000–800,000 years before present. *Nature* **453**, 379–382 (2008).

79. EPICA community members. Eight glacial cycles from an Antarctic ice core. *Nature* **429**, 623–628 (2004).
80. Ganopolski, A. & Calov, R. The role of orbital forcing, carbon dioxide and regolith in 100 kyr glacial cycles. *Clim. Past* **7**, 1415–1425 (2011).
81. Hammer, O. *Paleontological Statistics (PAST) version 3.21 reference manual*. https://folk.uio.no/ohammer/past/ (2018).
82. Torrence, C. & Compo, G. P. A practical guide to wavelet analysis. *Bull. Am. Meteorol. Soc.* **79**, 61–78 (1998).
83. Wagner, B. et al. The last 40 ka tephrostratigraphic record of Lake Ohrid, Albania and Macedonia: a very distal archive for ash dispersal from Italian volcanoes. *J. Volcanol. Geotherm. Res.* **177**, 71–80 (2008).
84. Zanchetta, G. et al. Tephrostratigraphy, chronology and climatic events of the Mediterranean basin during the Holocene: an overview. *Holocene* **21**, 33–52 (2011).
85. Siani, G., Sulpizio, R., Paterne, M. & Sbrana, A. Tephrostratigraphy study for the last 18,000 ^{14}C years in a deep-sea sediment sequence for the South Adriatic. *Quat. Sci. Rev.* **23**, 2485–2500 (2004).
86. Albert, P. G. et al. Revisiting the Y-3 tephrostratigraphic marker: a new diagnostic glass geochemistry, age estimate, and details on its climatostratigraphical context. *Quat. Sci. Rev.* **118**, 105–121 (2015).
87. Satow, C. et al. A new contribution to the Late Quaternary tephrostratigraphy of the Mediterranean: Aegean Sea core LC21. *Quat. Sci. Rev.* **117**, 96–112 (2015).
88. Giaccio, B. et al. Isotopic (Sr–Nd) and major element fingerprinting of distal tephras: an application to the middle–late Pleistocene markers from the Colli Albani volcano, central Italy. *Quat. Sci. Rev.* **67**, 190–206 (2013).
89. Petrosino, P., Jicha, B. R., Mazzeo, F. C. & Russo Ermolli, E. A high resolution tephrochronological record of MIS 14–12 in the Southern Apennines (Acerno basin, Italy). *J. Volcanol. Geotherm. Res.* **274**, 34–50 (2014).
90. Marra, F., Karner, D. B., Freda, C., Gaeta, M. & Renne, P. Large mafic eruptions at Alban Hills Volcanic District (central Italy): chronostratigraphy, petrography and eruptive behavior. *J. Volcanol. Geotherm. Res.* **179**, 217–232 (2009).
91. Lindhorst, K. et al. Sedimentary and tectonic evolution of Lake Ohrid (Macedonia/Albania). *Basin Res.* **27**, 84–101 (2015).
92. Le Bas, M. J., Le Maitre, R. W., Streckeisen, A., Zanettin, B. & IUGS Subcommission on the Systematics of Igneous Rocks. A chemical classification of volcanic rocks based on the total alkali-silica diagram. *J. Petrol.* **27**, 745–750 (1986).
93. Melard, G. Algorithm AS 197: a fast algorithm for the exact likelihood of autoregressive-moving average models. *Appl. Stat.* **33**, 104–114 (1984).
94. Zanchetta, G. et al. Aligning and synchronization of MIS5 proxy records from Lake Ohrid (FYROM) with independently dated Mediterranean archives: implications for DEEP core chronology. *Biogeosciences* **13**, 2757–2768 (2016).

Acknowledgements The Hydrobiological Institute in Ohrid (S. Trajanovski and G. Kostoski) and the Hydrometeorological Institute in Tirana (M. Sanxhaku and B. Lushaj) provided logistic support for site surveys and the scientific drilling campaign. Drilling was carried out by Drilling, Observation and Sampling of the Earth's Continental Crust (DOSECC). A. Skinner provided logistic and technical advice before and during the drilling operation. The Scientific Collaboration on Past Speciation Conditions in Lake Ohrid (SCOPSCO) drilling project was funded by the International Continental Scientific Drilling Program (ICDP), the German Ministry of Higher Education and Research, the German Research Foundation, the University of Cologne, the British Geological Survey, the INGV and CNR (both Italy), and the governments of the republics of North Macedonia and Albania. V. Scao collected the V5 tephra, which was ^{40}Ar/^{39}Ar dated with funding from the LEFE 'INTERMED' grant (CNRS-INSU) to S.N.

Author contributions B.W. and H.V. designed the study. B.W. initiated and coordinated the SCOPSCO drilling project and drilling campaign. H.V. conceived major scientific ideas for this study. A.F. (sedimentology, chronology), T.F. (LOVECLIM modelling), T.D. (palynology), J.H.L. (isotope geochemistry) and L. Sadori (palynology) contributed and oversaw key datasets used in the study and coordinated the discussion and interpretations of proxy data groups and model results together with F.W.-C., M.J.L., E.R., T. Wilke and G.Z. Specific data were provided by A.B. (pollen, MIS 19–21, MIS 25–28, MIS 42–43), N.C.-N. (pollen, MIS 1–4, MIS 8, MIS 14–15), B.G. (tephrostratigraphy), S.J. (pollen, MIS 1–4, MIS 13–16, MIS 30), J.J. (palaeomagnetic data), K.K. (pollen, MIS 6–8, MIS 10, MIS 16–19, MIS 28–30, MIS 33), I.K. (pollen, MIS 11–12, MIS 15), A.K. (pollen, MIS 11–12, MIS 15), M.L. (trace elements), N.L. (tephrostratigraphy), A.M. (pollen, MIS 5–6, MIS 20–25, MIS 31–32), A.M.M. (pollen, MIS 6, MIS 34), S.N. (tephrochronology), N.N. (palaeomagnetic data), K.P. (pollen, MIS 7–8, MIS 35–43), O.P. (pollen, MIS 1–4, MIS 13–16, MIS 30), L.Sagnotti (palaeomagnetic data), G.S. (pollen, MIS 5–6), R.S. (tephrostratigraphy) and P.T. (pollen, MIS 6, MIS 34). S.K., K.L. and T. Wonik coordinated the seismic survey of Lake Ohrid, the selection of the coring location and the geophysical measurements needed for core correlation. A.G., M.M., J.M.R. and Z.L. contributed to the conception of the work. A.C., J.H., E.J., S.T. and X.Z. provided micropalaeontological and organic geochemistry data, which confirmed that the sediment succession from the DEEP site covers the entire history of Lake Ohrid. A.T. provided model infrastructure and resources. All authors contributed to the discussion and interpretation of the data and provided comments and suggestions to the manuscript.

Competing interests The authors declare no competing interests.

Additional information
Correspondence and requests for materials should be addressed to B.W.
Peer review information *Nature* thanks Simon Blockley, Dirk Verschuren and Zhongshi Zhang for their contribution to the peer review of this work.
Reprints and permissions information is available at http://www.nature.com/reprints.

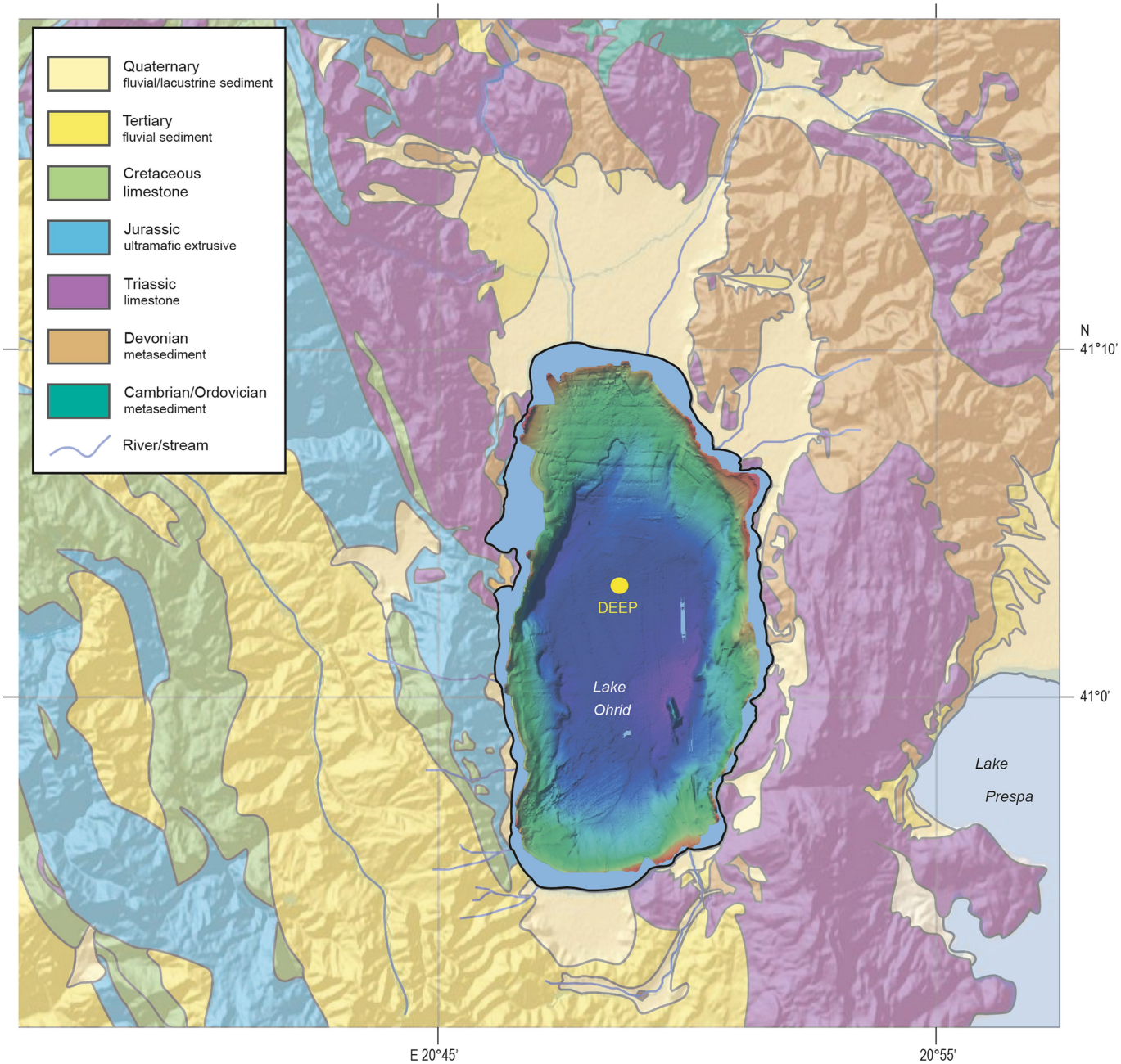

Extended Data Fig. 1 | Map of Lake Ohrid and its surrounding area. Geology, topography and bathymetry were compiled from previous studies[19,91] and geological maps of Albania and North Macedonia. The lake is located at an altitude of 693 m a.s.l. and has a maximum water depth of 293 m. The water depth at the DEEP drill site is 240 m.

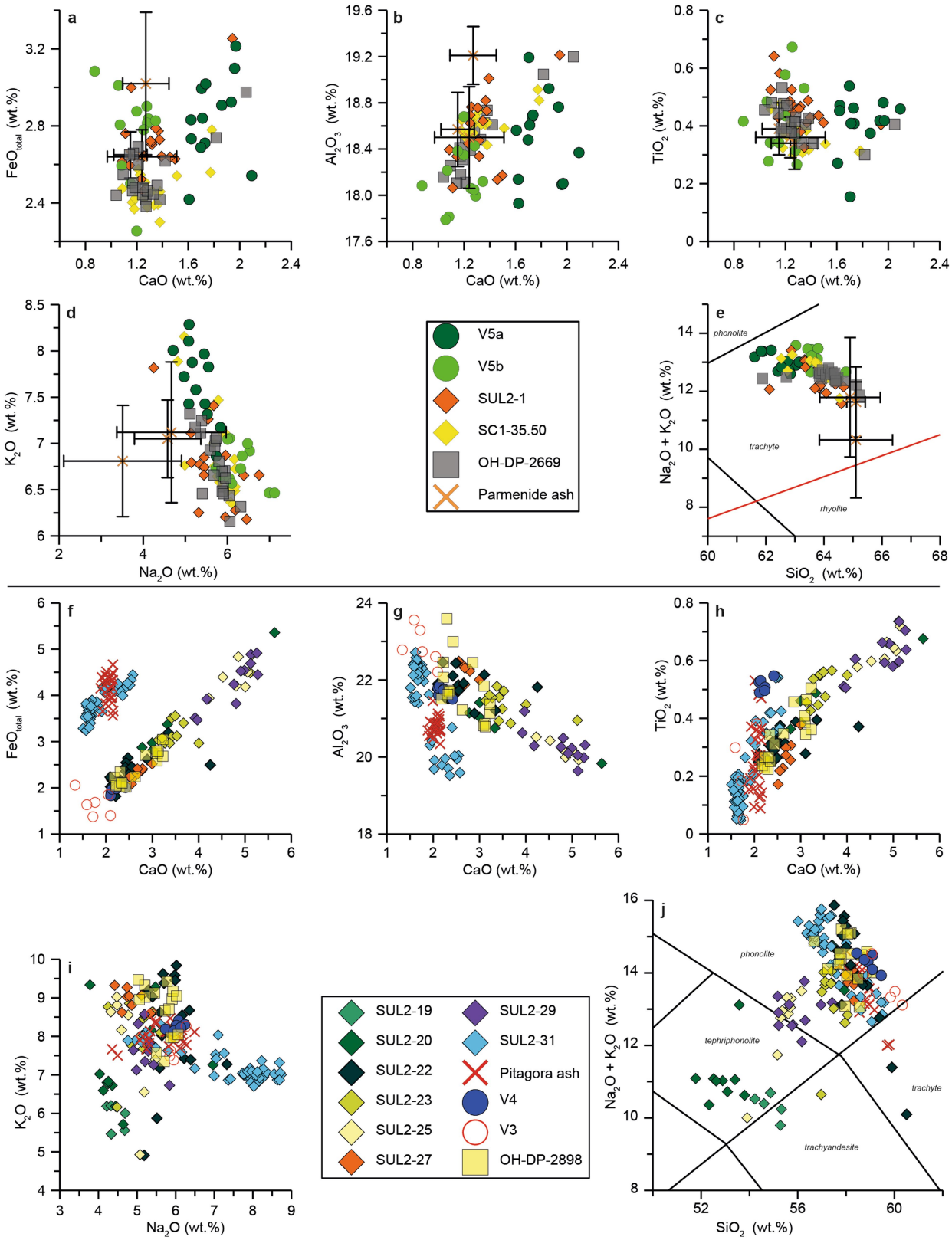

Extended Data Fig. 2 | Correlation of tephra layers at the DEEP site with tephra layers from mid-distal records. a–e, Bi-oxide plots of CaO versus FeO_{total} (**a**), CaO versus Al_2O_3 (**b**), CaO versus TiO_2 (**c**), Na_2O versus K_2O (**d**) and a total alkali versus silica diagram[92] (**e**) show the correlation of OH-DP-2669 with the tephra layers SC1-35.30/SUL2-1/V5 and the differences to the Parmenide ash. **f–j**, Bi-oxide plots of CaO versus FeO_{total} (**f**), CaO versus Al_2O_3 (**g**), CaO versus TiO_2 (**h**), Na_2O versus K_2O (**i**) and total alkali versus silica diagram (**j**) show the correlation of OH-DP-2898 with tephra SUL2-22 and the differences to SUL2-23, SUL2-27, SUL2-31, V4, V3 and the Pitagora ash. Error bars for the data of the Parmenide ash indicate the standard deviation[54]. Tephra ages, geochemical data, tephrostratigraphic discussion and references are provided in Extended Data Tables 1, 2 and the Methods.

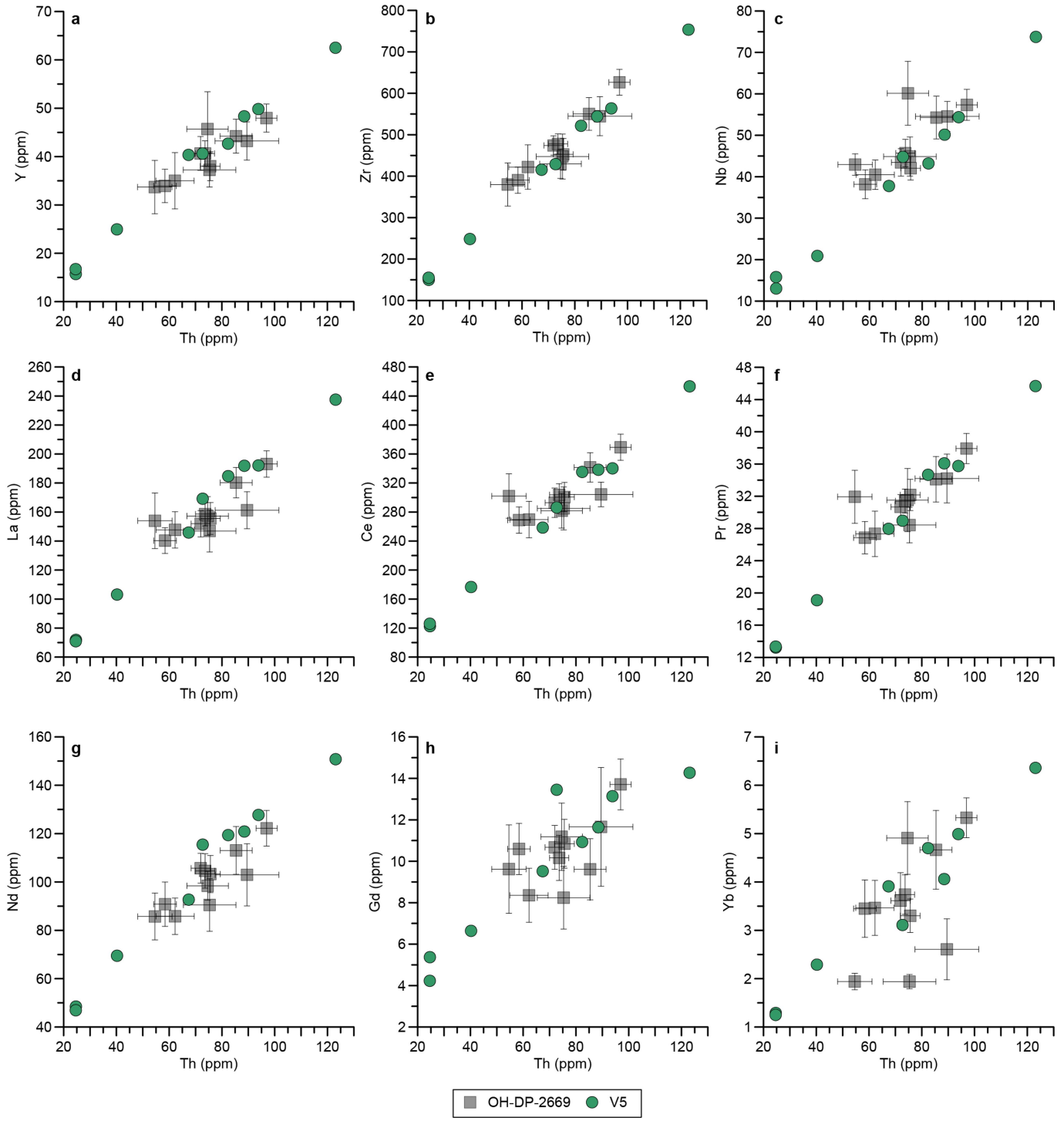

Extended Data Fig. 3 | Correlation of tephra layers OH-DP-2669 and V5 based on trace element compositions. Trace element data of OH-DP-2669 support the correlation with tephra V5a/b[52]. **a**, Th versus Y. **b**, Th versus Zr. **c**, Th versus Nb. **d**, Th versus La. **e**, Th versus Ce. **f**, Th versus Pr. **g**, Th versus Nd. **h**, Th versus Gd. **i**, Th versus Yb. Error bars for the data of OH-DP-2669 represent uncertainties at a 95% confidence interval. ppm, parts per million.

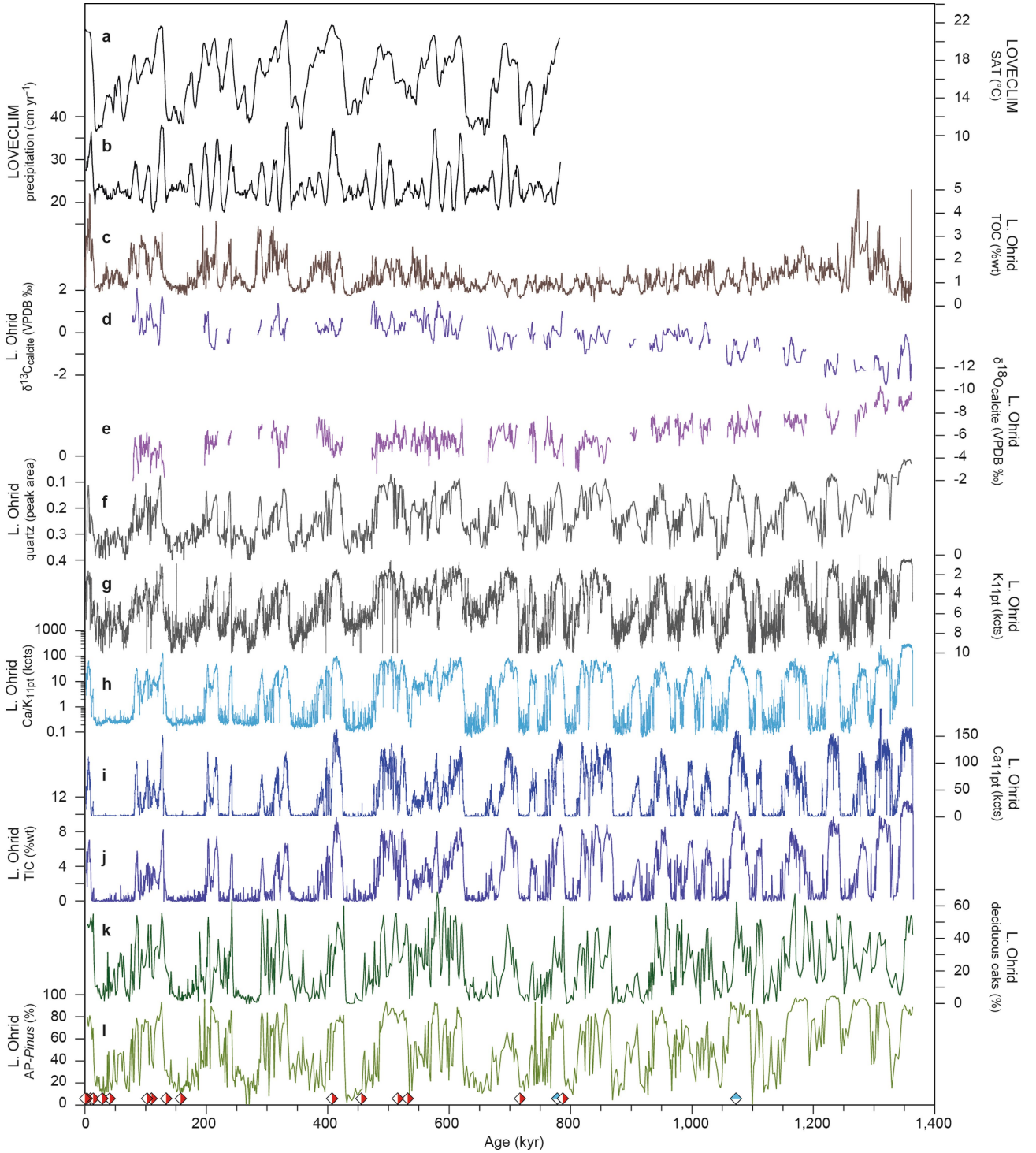

Extended Data Fig. 4 | Lake Ohrid LOVECLIM simulation data and sedimentary palaeoclimate and palaeoenvironment proxies. **a**, Simulated surface-air temperature (SAT) for the Lake Ohrid grid cell from the LOVECLIM simulation. **b**, Simulated precipitation amount for the Lake Ohrid grid cell from the LOVECLIM simulation. **c**, Lake Ohrid TOC concentrations. **d**, Lake Ohrid $\delta^{13}C$ endogenic calcite in parts per thousand relative to VPDB. **e**, Lake Ohrid $\delta^{18}O$ endogenic calcite in parts per thousand relative to VPDB. **f**, Lake Ohrid relative sedimentary quartz content. **g**, Lake Ohrid K intensities in kilo counts and displayed using a 11-point (pt) running mean. **h**, Lake Ohrid ratio of Ca/K intensities displayed using a 11-point running mean. **i**, Lake Ohrid Ca intensities in kilo counts and displayed using a 11-point running mean. **j**, Lake Ohrid TIC concentrations. **k**, Percentages of deciduous oak pollen at Lake Ohrid. **l**, Percentages of arboreal pollen excluding *Pinus* pollen at Lake Ohrid. Red and white diamonds indicate the position of radiometrically dated tephra layers, blue and white diamonds the position of reversals of Earth's magnetic field in the Lake Ohrid sediment record. **b**, **d**, **e**, **j**–**l**, Data are the same as in Fig. 2.

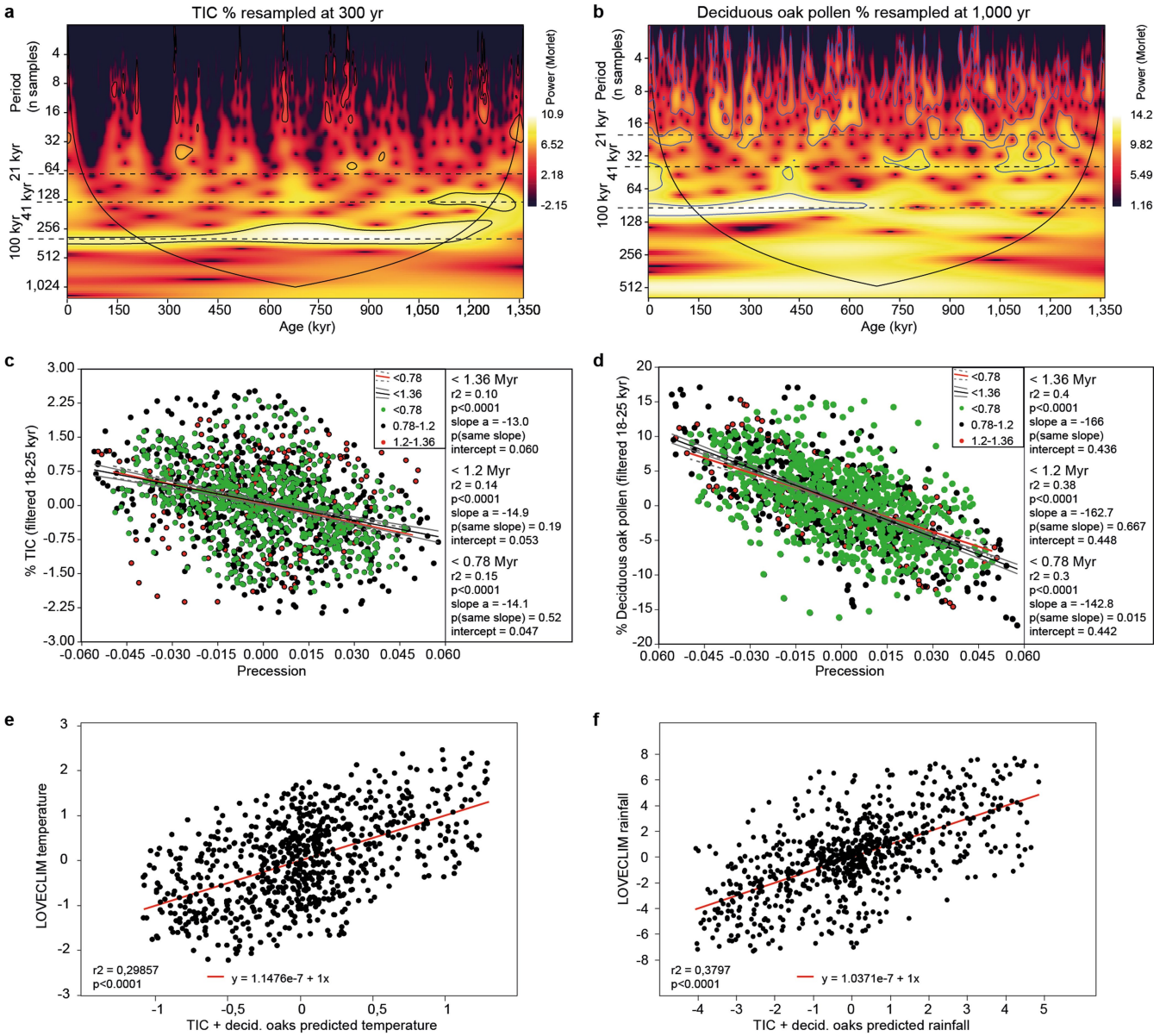

Extended Data Fig. 5 | Data analysis. a, **b**, Continuous wavelet transform on the percentage of TIC (**a**) and percentage of deciduous oak pollen (DOP; **b**) from Ohrid DEEP. Yellow, highest power; red, lowest power; grey contour, cone of influence; black contour, 5% significance level[82] against red-noise background corrected for autocorrelation[81,93]. **c**, **d**, Least squares regression (red line) between band pass-filtered 18–25-kyr-old component of percentage of TIC (**c**) and the percentage of DOP against precession at a 1-kyr resolution (**d**). Blue lines indicate 95% bootstrapped ($n = 1{,}999$) confidence intervals. Significant negative responses to precession are seen in both proxies, with a stronger response in DOP. Partial datasets for the intervals <0.78 Myr ago, <1.2 Myr ago, <1.36 Myr ago indicate persistence of the correlation despite changes in lake ontogeny and global scale changes in boundary conditions. **e**, **f**, PLSR using TIC and DOP as predictive variables and LOVECLIM temperature (**e**) and precipitation (**f**) simulations as observations demonstrate significant explanatory power by the proxies on the simulation time series, particularly for precipitation. PLSR was performed using SIMCA 14 (Sartorius Stedim Biotech), using 1.4–33-kyr bandpass-filtered data to accommodate for slight age offsets between proxy and simulation data.

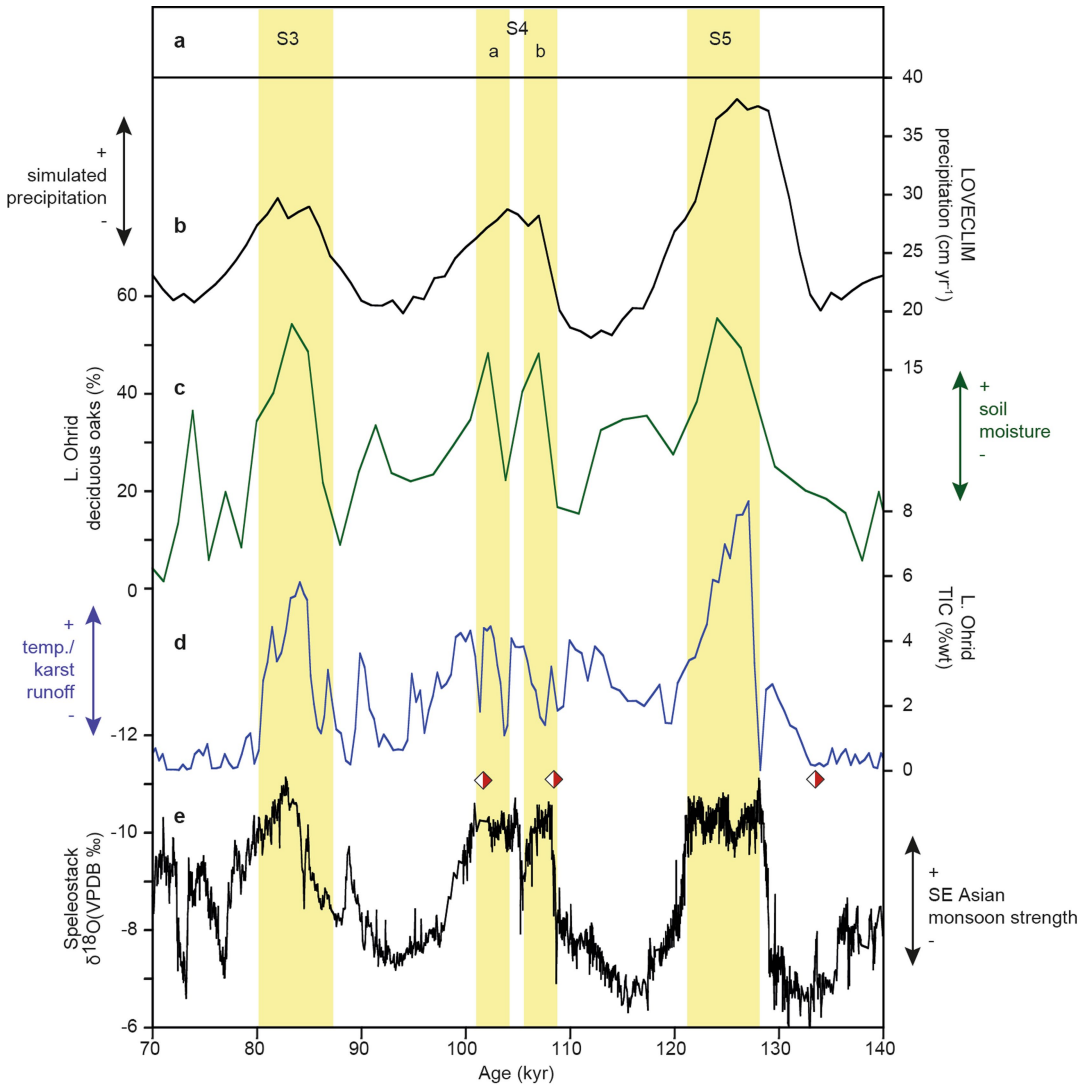

Extended Data Fig. 6 | Lake Ohrid precipitation indicators and global monsoon records during MIS 5. a, Ages of sapropels and humid phases in the eastern Mediterranean based on Soreq Cave speleothem $\delta^{18}O$ data and U/Th chronology[71]. **b**, Simulated precipitation amount for the Lake Ohrid grid cell from the LOVECLIM simulation. **c**, Percentage of deciduous oak pollen at Lake Ohrid. **d**, Lake Ohrid TIC concentrations. **e**, Chinese Speleostack[25] $\delta^{18}O$ in parts per thousand relative to VPDB. Red and white diamonds indicate the position of radiometrically dated tephra layers in the Lake Ohrid record. The chronology of the MIS 5 interval in the Lake Ohrid DEEP site record is based on a previous study[94].

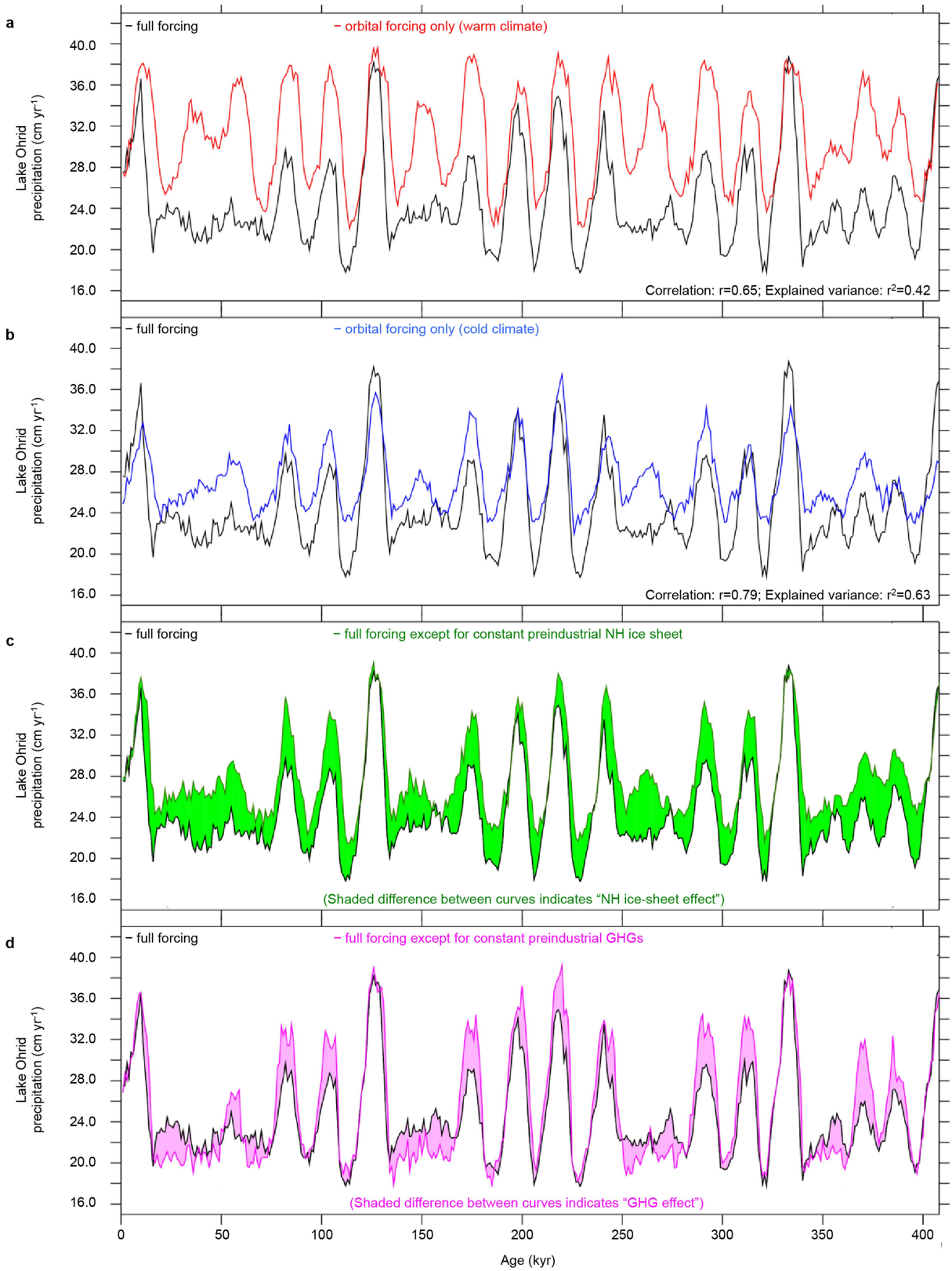

Extended Data Fig. 7 | Simulated Lake Ohrid precipitation for full-forcing run and sensitivity simulations. a, Lake Ohrid precipitation (cm yr^{-1}) for full-forcing simulation (black) and a simulation using only orbital forcing under a warm background climate (red). **b**, Black line as in **a** and a simulation using only orbital forcing under a cold background climate (blue). **c**, Black line as in **a** and a simulation using full-forcing except for a constant preindustrial Northern Hemisphere (NH) ice sheet. **d**, Black line as in **a** and a simulation using full-forcing except for constant preindustrial GHG concentrations. Note that the sensitivity simulations only cover the past 408 kyr (see Methods for details on the sensitivity simulations).

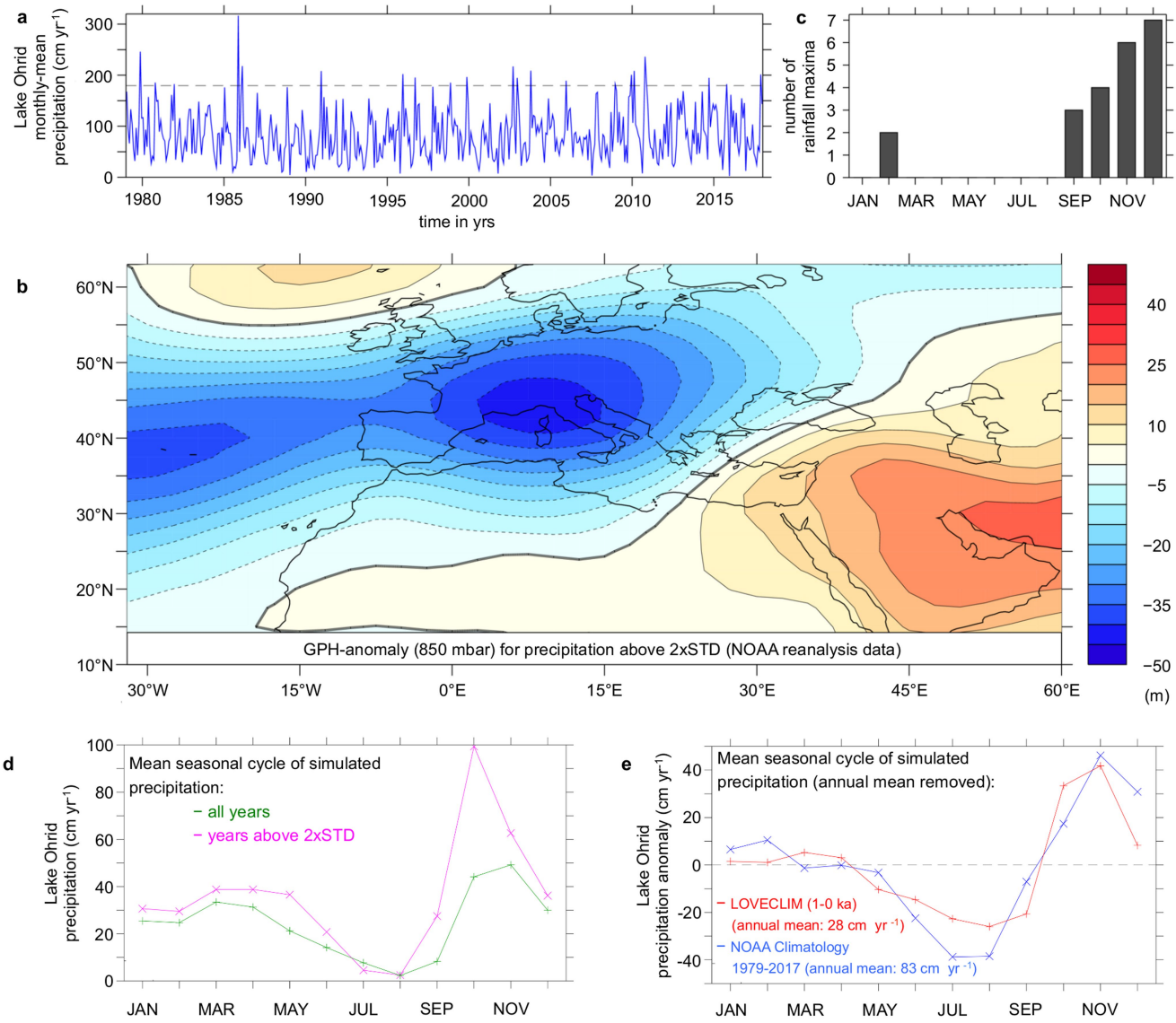

Extended Data Fig. 8 | Mean seasonal cycle of precipitation in the Lake Ohrid grid cell from LOVECLIM model simulation and NOAA reanalysis data. a, Reconstructed precipitation (cm yr^{-1}) for the Lake Ohrid reanalysis grid cell. Data are based on monthly means. Dashed line indicates two standard deviations above the mean. **b**, Composite anomalies of 850 hPa geopotential height (m) associated with Lake Ohrid precipitation maxima shown in **a** and referring to the months shown in **c**. **c**, Monthly distribution of precipitation maxima shown in **a**. **d**, Mean seasonal cycle of simulated Lake Ohrid precipitation (cm yr^{-1}) for all model years (green) and model years with annual mean precipitation exceeding two standard deviations (magenta). See also Fig. 3a. **e**, Mean seasonal cycle of Lake Ohrid precipitation (cm yr^{-1}) derived from NOAA reanalysis data (blue) and simulated for the period from 1 kyr ago to present (red). The annual means were removed for better comparison and are provided in the panel.

Extended Data Table 1 | Selected tephra layers from Lake Ohrid and their correlation with tephra layers of other records

Ohrid tephra	depth (m c.d.)	correlation	Reference	Reference age (kyr)	Recalculated age (kyr)
OH-DP-0009	0.904	AD512/472	historic	**1.46 ± 0.02**	N/A
OH-DP-0015	1.554	FL	87	**3.37 ± 0.07**	N/A
OH-DP-0027	2.773	Mercato	88	**8.53 ± 0.10**	N/A
OH-DP-0049	4.917	LN1	89	**14.75 ± 0.52**	N/A
OH-DP-0115	11.507	Y-3	90	**29.05 ± 0.37**	N/A
OH-DP-0169	16.933	Y-5	63	39.85 ± 0.12	**39.99 ± 0.12**
OH-DP-0404	40.486	POP2	64	**101.80 ± 1.80**	N/A
OH-DP-0435	43.513	X-6	64	109.50 ± 0.90	**109.20 ± 0.90**
OH-DP-0499	49.947	P-11	91	**133.50 ± 2.00**	N/A
OH-DP-0624	62.410	TF-17	65	158.80 ± 3.00	**158.29 ± 3.00**
OH-DP-1700.6	170.06	Vico β	67	410.00 ± 2.00	**414.03 ± 2.02**
OH-DP-1817	181.769	Pozzolane Rosse	92	457.40 ± 1.70	**455.94 ± 1.70**
OH-DP-2017	201.782	A11/12	93	514.20 ± 5.60	**515.96 ± 5.62**
OH-DP-2060	206.079	Tufo di Bagni Albule	94	527.00 ± 2.00	**532.18 ± 2.02**
OH-DP-2669	266.934	SC1-35.30/SUL2-1	50	717.30 ± 5.40	715.02 ± 5.40
		V5	this study	N/A	**716.20 ± 5.40**
OH-DP-2898	289.83	SUL2-22	58	791.90 ± 1.90	**789.38 ± 1.90**

$^{40}Ar/^{39}Ar$ ages from literature[50,58,63–65,67,83–90] were recalculated using a decay constant[48] and the ages of the ACs-2[47] of 1.1891 Myr or Fish Canyon sanidine[48] of 28.294 Myr. Tephra ages in bold are used for age–depth modelling in Fig. 1. Age uncertainties (95% confidence interval) are provided according to the original reference (Reference age).

Extended Data Table 2 | Average compositions of OH-DP-2669 and OH-DP-2898 and potential equivalent correlations

Tephra		SiO_2	TiO_2	Al_2O_3	FeO_t	MnO	MgO	CaO	Na_2O	K_2O	Cl	P_2O_5	SO_3	F	Total	$K_2O + Na_2O$	K_2O / Na_2O
OH-DP-2669	$\bar{x}$	64.10	0.41	18.47	2.55	0.19	0.41	1.30	5.73	6.76	0.42	0.07	0.16	0.22	95.99	12.49	1.19
n=20	S	0.72	0.05	0.28	0.14	0.04	0.10	0.23	0.30	0.32	0.11	0.03	0.04	0.09	0.53	0.20	0.11
SUL2-1	$\bar{x}$	63.55	0.47	18.46	2.73	0.22	0.41	1.30	5.57	6.69	0.42	0.06	0.10	0.26	92.99	12.26	1.22
n=21	S	1.00	0.07	0.39	0.17	0.07	0.09	0.19	0.60	0.46	0.12	0.04	0.03	0.09	1.22	0.63	0.19
SC1-35.50	$\bar{x}$	63.84	0.37	18.59	2.46	0.20	0.45	1.33	5.78	6.90	0.30	0.07	0.14	0.18	96.21	12.69	1.20
n=19	S	0.56	0.05	0.14	0.10	0.06	0.09	0.18	0.41	0.50	0.06	0.04	0.03	0.09	1.71	0.35	0.18
V5	$\bar{x}$	63.20	0.41	18.34	2.81	0.19	0.43	1.49	5.78	7.23	0.33	0.11	0.11	-	100.00	13.01	1.27
n=19	S	0.81	0.11	0.35	0.22	0.12	0.14	0.34	0.62	0.55	0.11	0.09	0.11	-	-	0.34	0.22
Parmenide ash	$\bar{x}$	65.03	0.36	18.76	2.77	0.17	0.43	1.22	4.25	6.99	-	-	-	-	100.00	11.25	1.67
n=?	S	0.87	0.08	0.34	0.21	0.09	0.16	0.19	1.16	0.59	-	-	-	-	-	1.76	0.51
OH-DP-2898	$\bar{x}$	58.06	0.34	21.76	2.41	0.14	0.27	2.67	5.64	8.67	0.23	0.03	0.10	0.55	93.90	14.37	1.54
n=16	S	0.58	0.09	0.77	0.33	0.03	0.11	0.40	0.34	0.65	0.03	0.04	0.05	0.10	0.96	0.62	0.18
SUL2-22	$\bar{x}$	58.46	0.31	21.79	2.36	0.17	0.23	2.57	5.84	8.22	0.24	0.05	0.13	0.42	92.69	14.06	1.41
n=19	S	0.76	0.05	0.34	0.30	0.05	0.11	0.51	0.51	1.28	0.03	0.04	0.06	0.13	1.79	1.41	0.24
SUL2-23	$\bar{x}$	57.36	0.53	21.37	3.29	0.20	0.37	3.61	5.04	8.19	0.20	0.04	0.15	0.45	93.22	13.23	1.63
n=11	S	0.35	0.08	0.31	0.43	0.06	0.10	0.53	0.39	0.74	0.07	0.03	0.03	0.16	1.59	0.93	0.18
SUL2-27	$\bar{x}$	58.27	0.27	22.26	2.32	0.19	0.17	2.70	4.83	8.97	0.24	0.03	0.12	0.55	92.40	13.80	1.87
n=8	S	0.16	0.06	0.20	0.13	0.05	0.04	0.14	0.27	0.25	0.02	0.02	0.02	0.10	0.95	0.26	0.14
V4	$\bar{x}$	58.96	0.52	21.71	1.96	0.04	0.33	2.20	6.03	8.26	0.57	-	0.33	-	100.00	14.29	1.37
n=6	S	0.31	0.02	0.11	0.07	0.04	0.03	0.11	0.16	0.09	0.07	-	0.09	-	-	0.21	0.03
V3	$\bar{x}$	59.49	0.20	22.86	1.67	0.10	0.18	1.76	5.74	7.89	0.47	0.12	0.18	-	100.00	13.63	1.38
n=6	S	0.60	0.14	0.44	0.24	0.08	0.23	0.26	0.38	0.43	0.04	0.09	0.15	-	-	0.48	0.14
Pitagora ash	$\bar{x}$	58.44	0.23	20.79	4.15	0.22	0.24	2.07	5.75	8.01	0.51	0.11	0.11	-	100.00	13.76	1.40
n=27	S	0.49	0.12	0.22	0.28	0.13	0.08	0.08	0.45	0.23	0.07	0.11	0.10	-	-	0.56	0.11

Data of SUL2-1, SUL2-22, SUL2-23, SUL2-27 were obtained from a previously published study[51]; SC1-35.50 data have been published previously[50]; data for V5, V4, V3, Pitagora ash have been published previously[52] and the Parmenide ash data were obtained from a previously published study[54]. $\bar{x}$, mean; S, standard deviation; *n*, number of analyses.